Bifurcation analysis of steady Rayleigh–Bénard convection in a cubical cavity with conducting sidewalls

By DOLORS PUIGJANER[1], JOAN HERRERO[2], CARLES SIMÓ[3] AND FRANCESC GIRALT[2]

[1] Dept. Eng. Informàtica i Matemàtiques, Univ. Rovira i Virgili, Tarragona, Catalunya, Spain.

[2]Dept. Enginyeria Quimica, Univ. Rovira i Virgili, Tarragona, Catalunya, Spain.

[3] Dept. Matemàtica Aplicada i Anàlisi, Univ. de Barcelona, Barcelona, Catalunya, Spain.

(Received)

Natural convection in a cubical cavity heated from below with perfectly conducting sidewalls has been investigated numerically. A parameter continuation procedure based on a Galerkin spectral method has been applied to obtain the bifurcation diagrams for steady flow solutions over the region $Ra \leqslant 1.5 \times 10^5$ at Prandtl numbers Pr=0.71 and 130. In both cases, the bifurcation diagrams are more complex than those previously reported for adiabatic sidewalls. Four and nine different convective solutions (without taking into account the solutions obtained by symmetry) that are stable over certain ranges of Ra have been respectively identified at Pr=0.71 and 130. The dependence of the bifurcation diagrams and the topology of the flow patterns on the Prandtl number is also stronger in the case of conducting sidewalls. Most of the flow patterns investigated tend to adopt double toroid-like topologies, as the Rayleigh number is increased. This is especially noticeable at Pr=130, where all flow patterns adopt double-toroid shapes that are superimposed to the characteristic topologies adopted at values of Ra slightly above the respective bifurcation points where they originate. At sufficiently high Ra the double-toroid pattern configuration prevails. This phenomenon, which was not previously observed in the case of adiabatic lateral walls, is related to the thermal activity of the sidewalls, which locally extract/supply relatively large amounts of heat from/into the fluid. Current predictions are consistent with experimental flow transitions and topologies reported in the literature. In addition, a complete bifurcation study in the two dimensional (Ra, Pr) plane has been carried out for a particular flow pattern that is stable at both Pr=0.71 and 130. Since the surface of Nu over the (Ra, Pr) plane presents several folds and cusps, different regions can be identified as a function of the number of particular realisations of the flow pattern, varying between zero and five. Three different regions of stability have been found for this particular flow pattern in the (Ra, Pr) plane within the range of parameters investigated, i.e., $Ra \leqslant 1.5 \times 10^5$ and $0.71 \leqslant Pr \leqslant 130$.

1. Introduction

Rayleigh–Bénard convection in confined enclosures is an extensively studied area (Yang (1988); Koschmieder (1993); Getling (1998); Bodenschatz, Pesch & Ahlers (2000)) because of its practical applications and theoretical relevance. Since, for certain simple geometries and thermal boundary conditions, it constitutes a fluid flow problem with well-established base solutions for the velocity and temperature fields, it provides an appropriate model for the study of hydrodynamic instabilities and subsequent flow bifurcations preceding the onset of turbulence. The first bifurcation, corresponding to the instability of the motionless conductive state and the onset of convection, occurs when the Rayleigh number reaches a critical value Ra_c. In the case of confined domains the critical Rayleigh number depends not only on the geometry but also on the thermal boundary conditions. Several numerical linear stability analyses report on variation of Ra_c with respect to the width/height and length/height aspect ratios for parallelepipedical cavities with either perfectly conducting (Davis 1967; Catton 1972; Mizushima & Nakamura 2003) or adiabatic lateral walls (Catton 1970; Gelfgat 1999). Although these studies also identify the flow pattern developed at Ra slightly above the critical value, numerical parameter continuation and bifurcation methods applied to the nonlinear governing equations are needed to study the flow transitions that occur as the Rayleigh number is increased.

Flows in cubical cavities are particularly interesting because the intrinsic symmetry of this geometry yields steady state solutions with more symmetries than those found in parallelepipedical enclosures (Leong, Hollands & Brunger (1999); Pallarès *et al.* (2001); Pepper & Hollands (2002); Mizushima & Nakamura (2003)). Furthermore, given a solution, several other solutions can be originated by the geometrical symmetries. Actually, the bifurcation analyses reported by Puigjaner *et al.* (2004, 2006) reveal that the bifurcation diagrams of steady flow patterns that develop inside a cubical cavity with adiabatic lateral walls and filled either with air (Pr=0.71) or silicone oil (Pr=130) are rather complex. Five and six flow patterns (skipping the ones due to the symmetries of the problem) were respectively identified to be stable over some ranges of the Rayleigh number within the region $Ra \leqslant 1.5 \times 10^5$ at Pr=0.71 and 130. On the other hand, different steady flow patterns and several flow transitions were experimentally observed by Pallarès *et al.* (2001) in a cubical cavity filled with silicone oil (Pr=130) with both adiabatic and perfectly conducting lateral walls. Most of the experimental flow transitions between different steady flow patterns observed by these authors over the region $Ra \leqslant 8 \times 10^4$ and adiabatic lateral walls were explained by the bifurcation diagram reported in Puigjaner *et al.* (2006). The natural convection benchmark study reported by Leong, Hollands & Brunger (1998) was motivated by the discrepancies between numerical and experimental results or even between different experiments performed in similar conditions. They conclude that the natural convection of air inside a cubical cavity with perfectly conducting lateral walls was the most suitable physically-realisable problem for testing computational fluid dynamics codes against experimental results.

The difficulty to built up an experimental set-up with either perfectly adiabatic or perfectly conducting lateral walls may explain part of the discrepancies between computed and measured results for convection in cavities. One consequence of the lateral walls conduction is that part of the heat transferred from the bottom to the top wall flows through the lateral walls. The effect of the sidewall conductivity on the heat transport characteristics of confined turbulent flows was theoretically investigated by Ahlers (2000) and Roche *et al.* (2001). Both authors proposed definitions of the Nusselt number that take into account the rate of total heat transferred through the lateral walls. On the other hand, the effects of a sidewall with finite thermal conductivity on flows confined in a cylindrical cavity were numerically studied by Verzicco (2002). This author expressed the thermal boundary conditions as a function of the heat conductivity of the sidewall, which varied from adiabatic to high conducting. Verzicco (2002) showed that the heat conductivity of the sidewall not only affected the Nusselt number but also the topology of the mean flow structures which were modified compared to the ideal adiabatic sidewall flow. These differences in the topology of the flow structures when boundary conditions are changed from perfectly adiabatic to perfectly conductive, showed up in a clear way in our study and will be described in §3.

The aim of the present work is to determine the bifurcation diagrams of steady convective flow patterns in a cubical cavity with perfectly conducting lateral walls at both Pr=0.71 and 130 over the region $Ra \leqslant 1.5 \times 10^5$. The stability and domains of existence of the alternative steady solutions that arise at bifurcation points are depicted. Stable and unstable steady solution branches are tracked using an arclength continuation algorithm applied to the nonlinear steady governing equations obtained by means of a Galerkin method. Both steady and Hopf bifurcation points are determined along the different bifurcating branches. Initially unstable steady flow patterns are also tracked since they can become stable as a consequence of subsequent bifurcations (see Puigjaner *et al.* 2004, 2006). The study of the evolution of spatial configuration of flow patterns as Ra is increased focuses on those flow patterns that are stable over certain ranges within the studied domain. Since the evolutions of the flow patterns may be quite different from those reported by Puigjaner *et al.* (2004, 2006) for adiabatic lateral walls, the effect of thermal boundary conditions on the flow and heat transport characteristics was analysed for different flow patterns. On the other hand Puigjaner *et al.* (2006) showed that the dependence of the flow patterns and heat transport characteristics on the Prandtl number was significant but smooth when adiabatic lateral walls were assumed. To illustrate the complex dependence of the current bifurcation diagrams on Pr a comprehensive bifurcation study in the two dimensional (Ra,Pr) parameter plane is presented for one stable flow pattern. Moreover, predicted flow patterns and transitions are compared with the experimental results reported by Leong *et al.* (1999) at Pr=0.71 and Pallarès *et al.* (2001) at Pr=130.

2. Governing equations and numerical method

2.1. *Governing equations*

The problem of an incompressible flow of a Newtonian fluid confined in a cubical cavity with six rigid walls is investigated. The top and the bottom horizontal walls are kept at the constant temperatures T_c and T_h ($T_c < T_h$), respectively and the lateral walls are assumed to be perfectly conducting, that is a linear vertical temperature profile is assumed. The non-dimensional domain scaled by the length of the cubical cavity, L, is represented by $D = [-1/2, 1/2] \times [-1/2, 1/2] \times [-1/2, 1/2]$.

The problem is governed by mass conservation, Navier–Stokes and energy conservation equations. The non-dimensional equations depend on two dimensionless parameters, the Rayleigh number, Ra, and the Prandtl number, Pr, which control the physics and, hence, the solutions of the problem. These parameters are defined as $Ra = \beta(\Delta\theta)gL^3/\alpha\nu$ and $Pr = \nu/\alpha$, where g is the acceleration of gravity, β is the coefficient of thermal expansion, ν is the kinematic viscosity, α is the thermal diffusivity and $\Delta\theta = T_h - T_c$. Assuming the Boussinesq approximation, i.e., assuming that all fluid properties are constant except for a linear variation of density (ρ) with temperature in the buoyancy term of the Navier–Stokes equations, the governing dimensionless nonlinear equations for the velocity $\boldsymbol{V} = (u, v, w)$, the temperature departure from the motionless conductive state, θ, and pressure, p, are

$$Pr^{-1}\left(\frac{\partial \boldsymbol{V}}{\partial t}+Ra^{1/2}(\boldsymbol{V}\cdot\boldsymbol{\nabla})\boldsymbol{V}\right)-\nabla^2\boldsymbol{V}-Ra^{1/2}\theta\,\boldsymbol{e}_z+\boldsymbol{\nabla}\,p=0\,, \qquad (2.1a)$$

$$\frac{\partial\theta}{\partial t}+Ra^{1/2}(\boldsymbol{V}\cdot\boldsymbol{\nabla})\theta-\nabla^2\theta-Ra^{1/2}w=0\,, \qquad (2.1b)$$

$$\boldsymbol{\nabla}\cdot\boldsymbol{V}=0\,, \qquad (2.1c)$$

subject to boundary conditions

$$\boldsymbol{V}=\theta=0 \text{ at } |x|=|y|=|z|=1/2\,. \qquad (2.1d)$$

In (2.1 a) $\boldsymbol{e}_z$ denotes the unit vector in the z direction. The dimensionless equations (2.1 a–d) are obtained by taking $q_0=[\beta(\Delta\theta)gL\alpha/\nu]^{1/2}$, $\Delta\theta$, L^2/α and $\rho\nu q_0/L$ as characteristic scales for velocity, temperature, time and pressure, respectively,

It is worth to note that both the governing equations and the cubical geometry present several symmetry properties. Equations (2.1 a–d) do not change either when x and u are respectively replaced by $-x$ and $-u$ or when y and v are respectively replaced by $-y$ and $-v$. These equations also remain unchanged when z, w and θ are respectively replaced by $-z$, $-w$ and $-\theta$. In addition, any particular solution of (2.1 a–d) can be transformed into another solution by exchanging (x,y,z) and (u,v,w) by (y,x,z) and (v,u,w), respectively, due to the symmetry of the cubical geometry. Consequently, once a particular solution of (2.1 a–d) has been identified fifteen more solutions can be generated by using the symmetry properties of equations and geometry. These fifteen solutions are different unless the solution itself verifies one or more of those symmetry properties characteristic of the problem. In the current work the ensemble of all of these (up to sixteen) equivalent solutions is referred to as a *flow pattern*. On the other hand, a flow pattern is not to be understood as a unique or point solution of (2.1 a–d) for one particular value of the Rayleigh and Prandtl numbers but as the set of all point solutions that spans a certain range in Ra and Pr. Any two point solutions of (2.1 a–d) will belong to the same flow pattern if a continuation path between them exists in the (Ra, Pr) parameter plane and if no portion of such path needs to be generated as a result of a bifurcation other than turning points.

2.2. *Numerical Method*

The continuation procedure reported by Puigjaner *et al.* (2004) has been applied to determine the bifurcations and stability of the steady solutions ($\partial \boldsymbol{V}/\partial t = 0, \partial\theta/\partial t = 0$) of equations (2.1 a–d). This procedure, which is briefly described in this section, was based on a Galerkin spectral method with a complete, divergence-free set of basis functions satisfying all boundary conditions. A formulation of the velocity field in terms of three scalar potential functions (see Kessler 1987; Puigjaner *et al.* 2004) was used to obtain an appropriate set of divergence-free basis functions to expand the velocity vector field $\boldsymbol{V}$.

The velocity and temperature fields were approximated by the truncated expansion

$$\begin{pmatrix} \boldsymbol{V} \\ \theta \end{pmatrix} = \sum_{i=1}^{N_x}\sum_{j=1}^{N_y}\sum_{k=1}^{N_z}\sum_{s=1}^{4} a_{ijk}^{(s)} \boldsymbol{G}_{ijk}^{(s)} , \tag{2.2}$$

where $a_{ijk}^{(s)}$ are the unknown time-dependent coefficients, and $\boldsymbol{G}_{ijk}^{(s)}$ are defined as

$$\boldsymbol{G}_{ijk}^{(1)} = \begin{pmatrix} 0 \\ -g_i(x)f_j(y)f'_k(z) \\ g_i(x)f'_j(y)f_k(z) \\ 0 \end{pmatrix}, \quad \boldsymbol{G}_{ijk}^{(2)} = \begin{pmatrix} -f_i(x)g_j(y)f'_k(z) \\ 0 \\ f'_i(x)g_j(y)f_k(z) \\ 0 \end{pmatrix}, \tag{2.3a,b}$$

$$\boldsymbol{G}_{ijk}^{(3)} = \begin{pmatrix} -f_i(x)f'_j(y)h'_k(z) \\ f'_i(x)f_j(y)h'_k(z) \\ 0 \\ 0 \end{pmatrix}, \quad \boldsymbol{G}_{ijk}^{(4)} = \begin{pmatrix} 0 \\ 0 \\ 0 \\ g_i(x)g_j(y)g_k(z) \end{pmatrix}. \tag{2.3c,d}$$

The functions with superindex $s = 1, 2, 3$ refer to velocity components, while $s = 4$

concerns the temperature. In (2.3 a–d) the functions f are the so-called beam functions documented by Harris & Reid (1959), and the functions g and h are the trigonometric functions

$$\left.\begin{array}{llll} g_k(x): & \cos((2k-1)\pi x) & \text{or} & \sin(2k\pi x)\,, \\ h_k(x): & \cos(2(k-1)\pi x) & \text{or} & \sin((2k-1)\pi x)\,. \end{array}\right\} \qquad (2.4)$$

The values of N_x, N_y, N_z used in the actual computations are, typically, of the form $2m$ (it is useful to consider the parity of the functions) with $m = 7$. This gives a total set of $4 \times 14^3 = 11\ 076$ basis functions.

Since the thermal boundary conditions assumed in the present work are different from those used in Puigjaner *et al.* (2004), the basis functions involved in the expansion of the temperature field were modified to fulfil implicitly the thermal boundary conditions defined in (2.1 d). Thus, in the present work, the temperature field was approximated by the expansion

$$\theta = \sum_{i,j,k} a^{(4)}_{ijk} g_i(x) g_j(y) g_k(z)\,. \qquad (2.5)$$

The Galerkin method transforms the partial differential equations (2.1 a-d) into a system of ordinary differential equations whose unknowns are the time-dependent coefficients used to expand the velocity and temperature fields. For steady solutions the problem reduces to the nonlinear vector equation

$$\boldsymbol{f}(\boldsymbol{c}, Ra, Pr) = 0\,, \qquad (2.6a)$$

with

$$f_j = \sum_i (L_{ji}(Ra)c_i) - Ra^{1/2} \sum_{i,n} (Q_{jin}(Pr)c_i c_n)\,, \qquad j = 1, \cdots, N\,. \qquad (2.6b)$$

The components c_i of the vector $\boldsymbol{c}$ in (2.6 b) are the unknowns and the matrices with components L_{ji} and Q_{jin} contain the coefficients of the linear and nonlinear terms, respectively (see Puigjaner *et al.* 2004).

Bifurcations and stability of steady flow patterns have been mostly determined as a function of Ra for a fixed value of the Prandtl number. Thus, the Rayleigh number has been taken as abscissa in the bifurcation diagrams and the change of behaviour of flow patterns has been studied as a function of it. Provided that at least one solution of (2.6 a) has been determined, an arclength continuation method has been used to calculate further solutions on the branch, until either $Ra = 1.5 \times 10^5$ is reached or the branch connects with another solution branch. The eigenvalue problem associated with the asymptotic stability of steady solutions along the different solution branches in the bifurcation diagram has been solved by means of the ARPACK implementation (Lehoucq & Sorensen 1996) of the Arnoldi method (Morgan 1996). Further details about the numerical procedure are described in Puigjaner *et al.* (2004) and Puigjaner (2005).

A bifurcation study in the two dimensional (Ra, Pr^{-1}) parameter plane has been also performed for one of the identified flow patterns. The arclength continuation method described in Puigjaner (2005) and used in Puigjaner *et al.* (2004, 2006) has been modified to allow the continuation parameter to be either Ra or Pr^{-1} while keeping the other parameter fixed. Then, starting from a known flow pattern, curves over the solution surface defined by $\boldsymbol{f}(\boldsymbol{c}, Ra, Pr) = 0$ have been tracked using the continuation method with either Ra or Pr^{-1} fixed values. Finally, the solution surface has been determined by interpolation of the computed solutions over a triangular grid. It has to be noticed that the inverse of the Prandtl number, (Pr^{-1}), turned out to be a more suitable parameter than Pr, both in the continuation procedure and in the graphical representation of the solution surface. Note that the steady counterpart of (2.1) has a well defined limit for $Pr^{-1} \to 0$.

2.3. *Accuracy assessment*

Results obtained with the Galerkin method have been compared with numerical solutions obtained using the same fourth order finite-difference solver as in Puigjaner *et al.* (2006). The finite difference calculations were initialised from the velocity and temperature fields given by the Galerkin-based continuation method at some discrete values of the Rayleigh number. The relative differences in Nusselt number between the Galerkin and the finite difference solutions are listed in tables 1 and 2 for those solutions that are stable over certain Ra ranges within the studied domain at Pr=0.71 and 130, respectively. These tables show that the maximum difference in Nusselt number between the Galerkin and the finite difference solutions is 3.3% at $Ra = 1.5 \times 10^5$ and Pr=0.71.

Table 3 shows that the first bifurcation for the transition from the motionless conductive state to the onset of convection in the form of a stable x or y single roll, denoted as B_1, is predicted at $Ra = 6\,799$. This value is in good agreement with numerical (Catton 1970; Mizushima & Matsuda 1997) and experimental (Leong *et al.* 1998) values previously reported in the literature. This table also shows that current predictions for the values of Ra where the second and third bifurcations from the conductive state occur, respectively yielding a single toroid B_4 and a four interconnected half–rolls B_3, differ by 1% and 0.03% from those reported by Mizushima & Matsuda (1997). It should be remarked that linearization of (2.6 a) around the motionless conductive solution makes that bifurcations from the conductive state independent of the Prandtl number. Hence, the bifurcation values listed in table 3 are valid for both Prandtl numbers, Pr=0.71 and 130, investigated in the present work.

3. Results and discussion

Bifurcation diagrams at both Pr=0.71 and 130 are first presented and the spatial configuration of stable flow patterns and their evolution as Ra is increased are discussed. The effect of sidewall conductivity on heat transport characteristics, which might be the reason for the disagreement between different experimental results, is then analysed by comparing current results with those previously obtained when adiabatic lateral walls are assumed. This is followed by a comparison of present results with the experimental studies of Leong *et al.* (1999) at Pr=0.71 and Pallarès *et al.* (2001) at Pr=130. Finally, the dependence of a particular stable flow pattern on both the Rayleigh and the Prandtl numbers is comprehensively analysed by performing a bifurcation study in the two dimensional (Ra, Pr^{-1}) parameter plane.

3.1. *Bifurcation diagrams and flow patterns at Pr=0.71 and 130*

Bifurcation diagrams display a scalar measure of the changes in the solutions of a set of equations as a function of one or more parameters. They are very useful to show the domains of existence, stability character and branching of the multiple solutions that may coexist as parameter are varied. In particular, the coexistence of several stable solutions for some ranges of parameters may yield hysteresis in time dependent simulations (or in physical experiments) when the parameters are increased or decreased stepwise. In the current section bifurcation diagrams depict the branches of steady flow patterns in the (Ra,Nu_h)-space for two fixed values of the Prandtl number, namely Pr=0.71 and 130. The Nusselt numbers Nu_h and Nu_c are respectively the dimensionless convective heat transport coefficients at the hot bottom and top cold plates and were calculated as,

$$Nu_h = 1 - \int_{-0.5}^{0.5}\int_{-0.5}^{0.5} \frac{\partial \theta}{\partial z}(x, y, -0.5)dx\,dy\,. \tag{3.1a}$$

$$Nu_c = 1 - \int_{-0.5}^{0.5}\int_{-0.5}^{0.5} \frac{\partial \theta}{\partial z}(x, y, 0.5)dx\,dy\,. \tag{3.1b}$$

In contrast to the case of adiabatic lateral walls (Puigjaner *et al.* 2004, 2006), the heat transferred through the hot bottom plate, Nu_h, and through the cold top plate, Nu_c, may not be necessarily the same when perfectly conducting lateral walls are assumed. These differences in Nu balance the heat transferred through the lateral walls. However, both Nusselt numbers are equal when the flow pattern presents symmetry characteristics that cause the net overall heat transfer rate of the sidewalls to be zero. The effect of sidewalls conductivity on heat transport characteristics is discussed in §3.2.

Bifurcations from the conductive state, are referred to as *primary bifurcations* and the term *secondary bifurcations* refers to bifurcations from convective flow solutions. The solutions branches depicted in the bifurcation diagrams discussed in this section have been initiated from solutions that set in at primary bifurcations. The values of Ra where primary bifurcations are predicted and the flow patterns developed are listed in table 4 for values of Ra up to 3×10^4. Those primary bifurcations where two different flow patterns arise correspond to double eigenvalues of the linearised problem. The brief descriptions of the flow patterns included in table 4 refer to their three dimensional spatial configuration at values of Ra close to the bifurcation value where they set in. Due to the independence of primary bifurcations on the Prandtl number these descriptions are valid for both Pr=0.71 and 130 at values of Ra near the corresponding primary bifurcation. However the evolution of flow patterns as Ra increases is rather dependent on Pr. Since the symmetry properties of flow patterns are useful to understand their spatial configuration, bases of the groups of symmetries are also included in table 4. The elements of the groups of symmetries associated to flow patterns are rotations around an axis, reflections with respect to a plane or combinations of both; they are represented by the 3×3 $\mathcal{S}$ matrix. Thus, if $\mathcal{S}$ belongs to the symmetry group of a flow pattern denoted as B then the transformations $\mathcal{S}\mathbf{X}$ and $\mathcal{S}\mathbf{V}$, with $\mathbf{X} = (x, y, z)$ and $\mathbf{V} = (u, v, w)$, do not change the flow pattern B. The matrices S_x, S_y, S_{d_+} and S_{d_-} denote reflections with respect to the $x=0$, $y=0$, $x=y$ and $x=-y$ planes, respectively. Their representations are

$$\mathsf{S}_x = \begin{pmatrix} -1 & 0 & 0 \\ 0 & 1 & 0 \\ 0 & 0 & 1 \end{pmatrix}, \quad \mathsf{S}_y = \begin{pmatrix} 1 & 0 & 0 \\ 0 & -1 & 0 \\ 0 & 0 & 1 \end{pmatrix}, \qquad (3.2a,b)$$

$$\mathsf{S}_{d_+} = \begin{pmatrix} 0 & 1 & 0 \\ 1 & 0 & 0 \\ 0 & 0 & 1 \end{pmatrix}, \quad \mathsf{S}_{d_-} = \begin{pmatrix} 0 & -1 & 0 \\ -1 & 0 & 0 \\ 0 & 0 & 1 \end{pmatrix}. \qquad (3.2c,d)$$

The symmetry with respect to the origin and a rotation of angle π around the y-axis are respectively denoted as $-\mathsf{I}$ and $-\mathsf{S}_y = -\mathsf{I}\cdot\mathsf{S}_y$, where I refers to the identity matrix.

Despite the present study is mainly focused on stable flow patterns, initially unstable flow patterns were also considered because they can become stable as a consequence of subsequent bifurcations. Specifically, those convective flow patterns having at most three (two) unstable eigenvalues near the primary (secondary) bifurcation point where they set in were tracked using the continuation method. In addition, when the solution branch being tracked by the continuation method ended at a bifurcation point of a different solution branch, this latter branch was also continued regardless of the number of unstable eigenvalues that it had.

Summaries of all identified flow patterns at both Pr=0.71 and 130 are presented in figures 1 and 2, respectively. In these figures, those flow patterns that are stable over certain ranges of Ra are printed in boldface. In addition, those solutions that represent the same flow pattern, i.e., those branches that in the bifurcation diagram connect two different bifurcation points, are joined by dashed arrows. The motionless conductive state is denoted by C, convective flow patterns that set in at primary bifurcations are labelled as B_i and flow patterns developed at bifurcation values of B_i are denoted as B_{ij}. The ranges of Ra where stable solutions exist and the ranges of Ra where they are stable are summarised in tables 5 and 6. Bases of the groups of symmetries associated to each flow pattern are also included in these tables. Whenever one, two, three or four of these symmetries coincide with the symmetries of the problem, i.e., the symmetries of (2.1 a–d) and cubical geometry, the number of different realisations of a flow pattern will be reduced from sixteen to eight, four, two or one, respectively. Only one particular solution of those sixteen that are related to the symmetry properties of the problem has been considered in the current work. Hence, the symmetry groups for the flow patterns listed in tables 4, 5 and 6 correspond to one particular solution. However, it is worth to note that two solutions related by the symmetry properties of (2.1 a–d) have exactly the same symmetry groups. The symmetry groups of two solutions related by the particular symmetry of the cubical geometry, which consists on respectively exchanging (x, y, z) and (u, v, w) by (y, x, z) and (v, u, w) are obtained by exchanging S_x by S_y and S_{d_+} by S_{d_-} in tables 4, 5 and 6.

3.1.1. *Cavity filled with air (Pr=0.71)*

For the sake of clarity the bifurcation diagrams presented in this section use the variable $Nu_h - 0.01Ra^{1/2}$ as ordinate instead of the Nusselt number Nu_h. Stable flow patterns are depicted with solid lines while unstable flow patterns are represented by dashed lines when they have exactly one unstable eigenmode and by dotted lines when they have two or more unstable eigenmodes. Steady, Hopf and saddle-node bifurcations are indicated with filled circles, hollow circles and hollow squares, respectively. The bifurcation diagram and the variation of the real part of the leading eigenvalues respectively depicted in figures 3 and 4 show that there are four steady flow patterns, denoted as B_1, B_3, B_{11} and B_{312}, which are stable over certain ranges of Rayleigh number for $Ra \leqslant 1.5 \times 10^5$. The ranges of

Ra where these solutions exist and the ranges of Ra where they are stable are summarised in table 5.

Table 5 shows that no stable steady solutions exist within the region $88\,205 \leqslant Ra \leqslant 90\,210$ at Pr=0.71. Direct numerical simulations performed with an explicit time–marching finite–difference solver (see Puigjaner *et al.* 2004) reveal that the time evolution of flow patterns is rather dependent on initial conditions over the region where no steady stable solutions develop. For example, for intermediate Rayleigh numbers within this region, the flow evolves towards a time periodic solution when the B_{11} flow pattern is used as initial condition, while it presents a chaotic behaviour when it is initiated with a motionless field and a temperature distribution linear in z. The existence of a time periodic solution is consistent with the destabilisation of the B_{11} flow pattern through a Hopf bifurcation shown in figure 3*a*. On the other hand, an examination of the chaotic time evolution shows that the flow approaches, at different times, two different unstable steady solutions and up to five different periodic solutions, all of them unstable. This chaotic behaviour suggests that connections between unstable and stable invariant manifolds of different unstable solutions (heteroclinic connections) occur. Moreover, these heteroclinic connections may, in turn, yield homoclinic connections, i.e., connections between the stable and the unstable manifold of the same solution. Future research will be oriented to the computation of unstable periodic solutions by using, for example, the Newton-Krylov approach (Sánchez *et al.* 2004), and of invariant manifolds that produce heteroclinic and homoclinic connections (Simó 1990).

As discussed in §2.3, the onset of convection is predicted at the critical value Ra_c=6 799, in agreement with the values reported in the literature (Catton 1970; Mizushima & Matsuda 1997; Leong *et al.* 1998). Previous numerical studies (Catton 1970; Mizushima & Matsuda 1997) did not take into account that the critical value corresponds to a double eigenvalue of the linear problem whose associated linear independent eigenvectors take the form of one x-roll and one y-roll, respectively. Consequently, they predicted that the flow pattern developed at the onset of convection was of the x- or y-roll type. In the current work all possible combinations of the two linear independent eigenvectors were considered as starting point to calculate possible emanating branches of solutions at the critical value and two solution branches, denoted as B_1 and B_2, were identified.

Since primary bifurcations are independent of Pr, the spatial configuration of flow patterns at Ra values close to their corresponding primary bifurcation points are very similar for any value of Pr. The method proposed by Jeong & Hussain (1995) to identify vortical structures has been used to characterise the spatial configuration of the flow patterns. These authors proposed to identify a vortex core as the connected region of negative λ_2, being λ_2 the second largest eigenvalue of $\mathcal{S}^2 + \Omega^2$, the sum of the squared symmetric and antisymmetric parts of the velocity gradient tensor. The surfaces $\lambda_2 = 0$ depicted in figure 5 for the B_1 and B_2 flow patterns at Ra=7 000 show that both flow patterns present a single roll spatial configuration when they set in. The B_1 and the B_2 flow pattern differ in the alignment of the single roll which is aligned in the y-axis direction (B_1) or in the positive diagonal direction (B_2). Figure 3a shows that the B_2 flow pattern is unstable over the whole range of Ra investigated. On the other hand, the B_1 solution is stable when it sets in but it becomes unstable due to a symmetry-breaking bifurcation that occurs at $Ra = 44\,700$, as shown in figures 3a and 4. Figure 6 shows that the B_1 solution at $Ra = 4.4 \times 10^4$ keeps its characteristic y-roll configuration but it has developed vortical structures parallel to two diagonally opposing edges of the cavity. Figure 7 shows that the unstable B_1 flow pattern at $Ra = 1.5 \times 10^5$ is quite different from both flow patterns shown in figures 5a and 6. Current B_1 presents two pairs of secondary rolls aligned in the x direction that originate near the top and bottom cavity walls.

An initially stable flow pattern, denoted as B_{11} (see figure 8), develops at the bifurcation point where the B_1 solution becomes unstable. This symmetry-breaking bifurcation is analogous to those previously reported by Puigjaner *et al.* (2004, 2006). Near the bifurcation point where the B_{11} flow pattern sets in it presents a spatial configuration similar to that of the stable solution B_1 plotted in figure 6, except for the loss of the central symmetry, denoted as $-I$ in table 5. However, as Ra is increased, the spatial configuration of the B_{11} flow pattern becomes more complex, as shown in figure 8. Whereas a y-roll configuration with a superposition of two relatively strong secondary vortical structures is adopted by B_{11} at the lower half of the cavity, the flow at the upper half presents a toroidal configuration. Figures 8 (b-d) show that at the upper half of the cavity air raises through the central part and sinks near the lateral walls with a stronger down-welling motion near the lateral wall $x = 0.5$. The B_{11} flow pattern becomes unstable at Ra=88 205 as a consequence of a Hopf bifurcation and remains unstable up to $Ra = 1.5 \times 10^5$, as shown in figures 3(a) and 4.

Figure 3(c) shows that the single toroidal flow pattern denoted as B_4 that develops at the second primary bifurcation (for adiabatic sidewalls the B_4 flow pattern develops at the third primary bifurcation) turns out to be unstable in the whole region investigated. Velocity contours and the surface $\lambda_2 = 0$, not shown here, reveal that this flow pattern presents a toroidal spatial configuration when it sets in. An initially unstable flow pattern denoted as B_3 sets in at the third primary bifurcation, predicted at Ra=11 612 (see table 3). Figure 9 shows that at values of Ra slightly above the bifurcation point, the B_3 flow pattern can be understood as four interconnected half rolls. As the Rayleigh number is increased secondary vortical structures parallel to the horizontal edges of the cavity are superimposed onto the characteristic four half rolls spatial structure of the B_3 solution, as shown in figure 10. The stability analysis indicates that regardless of the three real positive eigenvalues that characterise B_3 when it sets in, it becomes stable at Ra=90 210 and remains so thereafter, as shown in figures 3(b) and 4. Two of the three positive eigenvalues associated to the B_3 solution become negative at a double bifurcation point which takes place at Ra=14 350. At this bifurcation point two additional unstable flow patterns denoted as B_{31} and B_{32} arise. Figure 3(d) shows that the unstable flow pattern B_{31} connects the initially unstable B_3 solution with the solution denoted as B_{312}. Since the B_{312} solution branch forms a cycle two possible realisations of this flow pattern are possible over the range of Ra where it exists, except at the two turning points. It is worth to note that one of the two realisations of the B_{312} solution is stable over the range $22\,575 \leqslant Ra \leqslant 70\,683$, as shown in figures 3($d$) and 4. Figures 11 and 12 show that the stable realisation of the B_{312} flow structure (the upper branch in figure 3(d)) has essentially the configuration of the B_3 solution, including the secondary vortical structures that develop at the four vertical edges. However, there are two differences that are worth to note. The B_{312} solution has lost both reflection symmetries with respect the central planes $x = 0$ and $y = 0$, as indicated in table 5. Also, the B_{312} flow pattern tends to adopt a toroidal configuration in the upper half of the cavity.

3.1.2. *Cavity filled with silicone oil (Pr=130)*

The sketch of the bifurcation diagram presented in figure 2 shows that all solutions that set in at primary bifurcations, except for B_1, are connected to each other through their secondary bifurcations. As a consequence, the bifurcation diagram at Pr=130 cannot be broken up easily and, for the sake of clarity, only those solution branches that are stable over certain ranges in the studied domain are included in the bifurcation diagram depicted in figure 13. The bifurcation diagram and the variation of the real part of the leading eigenvalues respectively depicted in figures 13 and 14 show that there are nine steady flow patterns, denoted as B_1, B_2, B_3, B_5, B_{24}, B_{25}, B_{26}, B_{34} and B_{251}, which are stable over certain ranges of Ra in the region $Ra \leqslant 1.5 \times 10^5$. The ranges of Ra where these solutions exist and the ranges of Ra where they are stable are summarised in table 6.

Since primary bifurcations do not depend on the Prandtl number, solutions B_1, B_2, and B_3 correspond to the same flow structures previously discussed for Pr=0.71 when they set in at primary bifurcations. Thus, for Rayleigh numbers slightly above the bifurcation point these flow patterns present very similar topological structures at both Prandtl numbers. However, their subsequent bifurcations and the evolution of their spatial configuration is rather different. Figures 13(a) and 14 show that the B_1 flow pattern is stable when it sets in at the onset of convection but it becomes unstable as a consequence of a Hopf bifurcation that occurs at Ra=57 304. Hence, contrary to the Pr=0.71 case, the B_1 solution does not present the symmetry-breaking bifurcation where the steady B_{11} pattern arises. Furthermore, figure 15 shows that the B_1 flow pattern is no longer a single-roll, but it presents a double toroidal configuration even at moderate values of Ra. Thus, flow raises along the central part of the cavity and sinks near the lateral walls and vice-versa at the upper and bottom halves of the cavity, respectively, as shown in figures 15 (b-c). The upper toroid can be obtained from the bottom one by applying the central symmetry of the B_1 solution (see table 6). This symmetry explains why the centres of both toroidal structures in figures 15 (b-c) are shifted towards opposite lateral walls. In addition, figure 15(a) shows that both toroidal structures are connected in the central part of the cavity where the flow pattern corresponding to the basic y-roll spatial configuration remains, as shown in figure 15(b). The double toroidal configuration of the B_1 solution is even more evident as Ra increases up to Ra = 1.5×10^5, as shown in figure 16(a). The different spatial configuration of the B_1 flow pattern might explain the large Nusselt number of the B_1 solution at $Ra = 1.5 \times 10^5$ in figure 13(a) when compared with the corresponding Nu depicted in figure 3(a) for Pr=0.71. The relation between heat transfer rates and flow structure is discussed in §3.2.

In contrast to the results predicted at Pr=0.71, figures 13(b) and 14 show that the initially unstable B_2 diagonal roll solution becomes stable at Ra=67 730. The bifurcation point where the B_2 flow pattern becomes stable corresponds to a sub-critical bifurcation value, as shown in figure 13(b). This figure also indicates that the initially stable flow pattern, denoted as B_{24}, developed at this sub-critical bifurcation point becomes unstable as a consequence of a Hopf bifurcation occurring at Ra=67 713. Moreover, the B_2 solution becomes unstable, and a stable flow pattern, denoted as B_{25}, arises at the symmetry-breaking bifurcation point that takes place at Ra=85 694. Figure 13(b) shows that the flow pattern B_{25} connects the B_2 solution with the solution denoted as B_{251}. Thus, the B_{25} flow pattern exists only in the narrow region $85\,694 \leqslant Ra \leqslant 87\,598$, as shown in table 6. Since the B_{251} solution branch presents a turning point at Ra=48 116 two possible realisations of this flow pattern are possible for $Ra > 48\,116$. One of these two realisations is stable over both regions $61\,160 \leqslant Ra \leqslant 65\,297$ and $Ra \geqslant 87\,598$, as shown in Figures 13 and 14. The B_{26} solution arises at the bifurcation point of the B_2 solution that occurs at Ra=122 622. This solution, which is initially unstable, becomes stable at Ra=146 738 and remains so thereafter, as shown in Figure 13(b). The spatial configurations of the B_{24}, B_{25} and B_{26} flow patterns are shown in figures 16(b-d).

Figure 17 shows that the B_2 solution at $Ra = 8 \times 10^4$ is no longer a diagonal-roll, but, similarly to the B_1 solution discussed above, it adopts a double toroidal configuration. This figure shows that the upper and the bottom toroids can be obtained from each other by applying the central symmetry shown in table 6 to the B_2 flow pattern. As a consequence of the reflection symmetry with respect to the diagonal plane $x = -y$ the toroidal configuration of the B_2 solution is more complex than the one described for the B_1 flow pattern. Figures 16(b-d), 18 and 19 show that the B_{24}, B_{25}, B_{26} and B_{251} flow patterns have similar spatial configurations to that discussed for the B_2 solution at $Ra = 8 \times 10^4$, except for their different symmetry properties.

The initially unstable flow pattern B_3 that sets in at the third primary bifurcation point (Ra=11 612) becomes stable at Ra=20 637 and remains so until a secondary bifurcation takes place at Ra=79 362. The bifurcations and stability regions of the B_3 flow pattern are discussed in more detail in §3.4.

The flow pattern B_5, which sets in as an initially unstable flow pattern at the fourth primary bifurcation point, becomes stable at Ra=94 417 and remains so thereafter (at least up to Ra = 150 000). This stabilisation is not observed at Pr = 0.71 Figure 20 shows that at values of Ra slightly above the bifurcation point where it originates, the B_5 flow pattern presents the four interconnected half rolls configuration characteristic of the B_3 solution (see figure 9) but rotated an angle of $\pi/4$. It is worth to note that both the B_3 and the B_5 flow patterns evolve to a double toroidal configuration when Ra is increased, as shown in figures 21 and 22, respectively. Figure 13(b) shows that the B_3 and the B_5 solutions are connected through the stable flow pattern denoted as B_{34}. Specifically, the B_{34} solution connects the symmetry-breaking bifurcation point where the B_3 solution becomes unstable with the symmetry-breaking bifurcation point where the B_5 solution becomes stable. Consistent with these symmetry-breaking bifurcations, only two elements are needed to generate the symmetry group of the B_{34} flow pattern, as shown in table 6; the symmetry groups of both flow patterns B_3 and B_5 need three elements. This loss of symmetry is also evident in figure 23.

3.2. *Effect of sidewall conductance on heat transport characteristics*

The dimensionless rate of heat transfer from the hot bottom plate into the fluid, Nu_h, is equal to the rate of heat transferred between the fluid and the cold top plate, Nu_c, when the lateral walls are adiabatic. However, heat can also be transferred from the sidewalls into the fluid and vice-versa when conducting lateral walls are assumed. Consequently, the two Nusselt numbers Nu_h and Nu_c may be different in this case. Furthermore, the total input heat transfer, which includes the input heat transferred through the lateral walls, may differ from Nu_h for conducting lateral walls. The total dimensionless input heat transfer, denoted as Nu_t, is defined as

$$Nu_t = 1 + \langle \left(-\frac{\partial \theta}{\partial n} \cdot \boldsymbol{n} \right)^+ \rangle_{\partial D} \,, \tag{3.3}$$

where $\langle (f)^+ \rangle_{\partial D}$ indicates an average of the positive values of f over the boundary surface of the domain D and $\boldsymbol{n}$ refers to the unit vector normal to the boundary surface.

As an example, figure 24 shows the variation with of Nu_h, Nu_c and Nu_t with Ra for both the B_1 and the B_{11} flow patterns at Pr=0.71. The values of Nu_h and Nu_c are equal for the B_1 flow pattern in figure 24 due to its central symmetry property (see table 5), i.e., the symmetry of the B_1 flow pattern causes the net overall heat transfer rate of the sidewalls to be zero. In contrast, the initially stable flow pattern B_{11} yields different Nu at the two horizontal bottom and top plates to balance the heat exchanged through the lateral walls. The loss of the central symmetry property in the B_{11} solution, explains this difference in the heat transferred through the sidewalls. The total input heat transfer depicted in figure 24 shows the enhanced heat transfer ability of the B_{11} flow pattern compared to the B_1 solution.

The sidewalls effect can be quantified by comparing present Nusselt numbers, Nu_h, Nu_c and Nu_t, with the Nusselt number at the bottom hot plate obtained when the adiabatic boundary condition is applied, which is denoted as Nu_{ad}. Values of Nu_h, Nu_c, Nu_t and Nu_{ad} are reported in table 8 for the flow patterns B_1, B_{11}, B_2 and B_3 at several values of Ra and at both Pr=0.71 and 130. The factor $C = (Nu_h - Nu_{ad})/Nu_{ad}$, used by Verzicco (2002) to determine the effect of sidewall conductance on the heat transport in a cylindrical cavity, is also included in table 8. It is observed in this table that C is rather dependent on the particular flow pattern and takes greater absolute values for those flow patterns whose spatial configurations differ more from the corresponding ones for adiabatic lateral walls. Table 8 shows that the highest value of $\mid C \mid$ was obtained in the case of the B_1 flow pattern at $Ra = 1.5 \times 10^5$ and Pr=0.71. Note that the highest relative difference between Nu_t and Nu_h, denoted as F in table 8, was also reached in this case, indicating that differences in the flow patterns configurations between adiabatic and perfectly conducting lateral walls are related to the amount of heat transferred to the system through the lateral walls.

As pointed out by Verzicco (2002) for the case of a cylindrical cavity, the flow patterns characteristics are significantly affected by the heat transferred from the sidewall into the fluid and vice-versa. Figure 25 shows the profiles of the local Nusselt, Nu_l, at the three walls $x = 1/2$, $y = -1/2$ and $z = 1/2$ for the B_1 flow pattern at $Ra = 1.5 \times 10^5$ and both Pr=0.71 and 130. The local Nusselt number is defined by

$$Nu_l = -\frac{\partial \theta}{\partial n} \cdot \boldsymbol{n}\,. \tag{3.4}$$

Thus, regions of positive and negative Nu_l values in figure 25 respectively denote that fluid with negative or positive θ values is flowing near the wall surface. Thinking in these terms, it is not difficult to relate the Nu_l distributions in figure 25(*a1*, *b1*,*c1*) to the flow pattern portrayed in figure 7(a). Similarly, the distributions in figure 25(*a2*,*b2*,*c2*) are related to the corresponding flow pattern in figure 16(a). Figures 25(*a1*,*a2*) show that the fluid is relatively warm ($\theta > 0$) near the top plate but it is rapidly cooled as it drops along the sidewall boundary layer, as expected. These figures also reveal the presence of regions of fluid with $\theta > 0$ in the lower half of the cavity. Fluid motion in such regions corresponds to secondary rolls that are promoted by the conductive sidewalls, in the sense that fluid with positive (negative) values of θ can be kept in the bottom (top) half of the cavity only because heat is removed (supplied) through the sidewalls. The local Nusselt numbers in figure 25($b2$) reflect very well the characteristic double toroid flow configuration of the B_1 flow pattern at $Ra = 1.5 \times 10^5$ and Pr=130 portrayed in figure 16(a). Thus, since relatively warm fluid is cooled near the top wall, a down-welling motion arises along the vertical wall boundary layer where the fluid warms quickly. The opposite is true for relatively cold fluid near the bottom wall. The obvious way to accommodate these two opposite up- and down-welling motions that meet at about the horizontal midplane is the double toroid configuration depicted in figure 16(a). Note that this double toroid configuration is also adopted by other flow patterns, especially at Pr=130, as can be seen in figures 17(a) (B_2), 19(a) and 18(a) (B_{251}) and, even more clearly by the B_3 flow pattern in figure 21(a).

3.3. *Comparison with experiments*

Present results can be compared with the experimental studies reported by Leong *et al.* (1999) and Pallarès *et al.* (2001). Both experiments were performed in a cubical cavity with lateral walls approximating perfectly conducting boundary conditions. A sketch of the physical devices used in these experiments is shown in figure 26. Air (Pr=0.71) was used as fluid in the experiments of Leong *et al.* (1999), whereas the experimental cavity used by Pallarès *et al.* (2001) was filled with silicone oil (Pr=130). Pallarès *et al.* (2001) used the dimensionless number $\gamma = k_f L/(k_w d_w)$ to quantify the finite thermal conductivity of the sidewalls. In this expression k_f and k_w are respectively the thermal conductivities of the fluid and the walls, d_w is the thickness of the lateral walls and L

is the height of the cavity. The dimensionless number γ is equivalent to the inverse of the quantity denoted as W by Verzicco (2002). The value $\gamma = 0$ corresponds to perfectly conducting lateral walls. The values of γ corresponding to the experimental set-ups of Leong *et al.* (1999) and Pallarès *et al.* (2001) were respectively $\gamma = 0.0026$ ($L/d_w = 39.9, k_f/k_w = 6.5 \times 10^{-5}$) and $\gamma = 0.45$ ($L/d_w = 0.625, k_f/k_w = 0.72$). It is worth to mention that both adiabatic and perfectly conducting lateral walls were considered in the experimental work of Pallarès *et al.* (2001). Comparison between experimental and Galerkin numerical results in the case of adiabatic lateral walls has been already reported by Puigjaner *et al.* (2006).

3.3.1. *Cavity filled with air (Pr=0.71)*

Table 3 shows that the critical Rayleigh number predicted by the current work is in good agreement with the experimental value reported by Leong *et al.* (1999). Differences between current predictions and experimental Nusselt numbers are below 4% in all cases, as shown in table 7. This table also includes the name of the corresponding flow pattern predicted by the Galerkin method. It should be remarked that as a consequence of the symmetries discussed in §2.1 any flow pattern is equally realisable with either positive or negative sign of the x and y vorticity components. Present work predicts different values of Nu_h and Nu_c for the B_{11} flow pattern. Thus, it may be possible that the two different values of Nu reported by Leong *et al.* (1999) at $Ra = 10^5$ (see table 7) correspond to two different particular realisable shapes of the same flow pattern B_{11} that differ on the sign of the y vorticity. Actually, this explanation is consistent with the fact that Leong *et al.* (1999) reported that the Nu_c value of one solution coincided with the Nu_h value of the other and vice-versa. In addition, figure 27 shows that the velocity field obtained in the present work agrees qualitatively with that obtained numerically by these authors (see figure 5 of Leong *et al.* (1999) for comparison). These authors reported a steady B_{11}

flow pattern at $Ra = 10^5$. This value of the Rayleigh number is only slightly higher than the Ra=88 205 value where, according to present results, the B_{11} flow pattern becomes unstable as a consequence of a Hopf bifurcation.

3.3.2. *Cavity filled with silicone oil (Pr=130)*

The only flow patterns experimentally observed by Pallarès *et al.* (2001) in a cubical cavity with conducting lateral walls ($\gamma = 0.7$) and filled with silicone oil (Pr=130) in the range $5\times10^3 \leqslant Ra \leqslant 8\times10^4$ were those denoted as $S1$, $S2$ and $S5$ by these authors, which correspond to the current B_1, B_2 and B_3, respectively. The unstable toroidal flow pattern B_4, which was denoted as $S4$ by Pallarès *et al.* (2001), was experimentally identified in that work as a transitional state during the start-up of the experimental apparatus. This transitional B_4 flow pattern eventually evolved to the B_2 solution. Figure 28(a) shows the sequence of flow transitions from the B_2 solution to other steady flow patterns reported by Pallarès *et al.* (2001) when the Ra was increased or decreased. As Ra was increased the first transition, which corresponds to transition from the diagonal-roll B_2 to the single-roll B_1, was observed in the range $10^4 < Ra < 2 \times 10^4$. The second transition was observed in the range $5\times10^4 < Ra < 5.5\times10^4$ and made the B_1 solution evolve again towards the B_2 flow pattern. Finally, in the range $6 \times 10^4 < Ra < 6.5 \times 10^4$ a third transition from the B_2 solution to the B_3 flow pattern was experimentally identified. It was observed experimentally that once the B_3 flow pattern was developed, it remained stable when decreasing the Rayleigh number until the initial diagonal-roll B_2 was recovered at a value of Ra in the range $10^4 < Ra < 2\times10^4$. Furthermore, Pallarès *et al.* (2001) reported that a flow pattern, denoted as $S6$ by these authors, developed at $Ra = 1.2\times10^5$ and remained stable when the Rayleigh number was decreased to $Ra = 8 \times 10^4$.

The present study predicts that both the initially stable B_1 and the initially unstable B_2 flow patterns develop at the smallest primary bifurcation (Ra_c=6 798). It also predicts that the B_2 flow pattern remains unstable until a further bifurcation takes place at Ra=67 730, as observed in figure 13. Figures 28(a and b) show that the value of Ra where the transition from the B_1 solution to the B_2 solution was experimentally observed agrees with the current predicted value of Ra where the B_1 solution becomes unstable. However, the experimentally observed consecutive transitions from B_1 to B_2 and from B_2 to B_3 flow patterns in figure 28(a)are not found in the current work (figure 28(b)) where the B_1 solution becomes unstable as a consequence of a Hopf bifurcation, Notwithstanding, it is possible that the flow pattern found experimentally within the range $5.5 \times 10^4 \leqslant Ra \leqslant 6.5 \times 10^4$ was the B_{251} solution, which is predicted to be stable within the ranges $61\,160 \leqslant Ra \leqslant 65\,297$ and $Ra \geqslant 87\,598$, as shown in figure 29. Note that the spatial configuration of the B_{251} flow pattern at $Ra = 6.3 \times 10^4$ depicted in figure 18 is rather similar to that plotted in figure 17 for the B_2 solution at $Ra = 8 \times 10^4$. The current work predicts that the B_3 solution becomes stable at Ra=20 637, which is consistent with the experimentally observed stability of this solution when decreasing the Rayleigh number up to $Ra = 2 \times 10^4$. In addition, the spatial structure of the flow pattern B_5, shown in figure 20, and its region of stability ($Ra \geqslant 94\,417$), suggest that the solution denoted as $S6$ by Pallarès *et al.* (2001) might correspond to the current B_5 flow pattern. This hypothesis is reinforced by the connection between the B_3 and the B_5 solutions in the bifurcation diagram depicted in figure 13(b).

3.4. *Effect of the Prandtl number*

Comparison of the bifurcation diagrams respectively presented in figures 3 and 13 for Pr=0.71 and 130 reveal that the evolution of the flow patterns as Ra is varied, their stability character, and their subsequent bifurcations depend strongly on the Prandtl number. Accordingly, the spatial configurations of flow patterns at Pr=130 are rather different from the corresponding ones at Pr=0.71. Present results reveal that, in contrast to the case of air (Pr=0.71), flow patterns tend to adopt a double toroid configuration as Ra is increased when the cavity is filled with silicone oil (Pr=130). In addition, considerable differences in the regions of stability of the B_2, B_3 and B_5 flow patterns are also evident when tables 5 and 6 are compared. In particular, these tables show that both the B_2 and B_5 flow patterns are unstable over the whole region $Ra \leqslant 1.5 \times 10^5$ at Pr=0.71, but they are stable over some ranges within the studied domain at Pr=130.

To better illustrate the effect of the Prandtl number the B_3 flow pattern, which shows completely different regions of stability at Pr=0.71 and 130, was chosen to perform a more exhaustive bifurcation study in the two dimensional (Ra, Pr) parameter plane. The three dimensional surface plotted in figure 30 shows the variation of the Nusselt number for the B_3 solution as a function of the two control parameters Ra and Pr^{-1}. The presence of folds in this figure indicates that several realisations of the B_3 flow pattern are possible for some values of Ra and Pr^{-1}. The parameter chart plotted in figure 31 shows the regions in the (Ra,Pr) parameter plane where different number of flow realisations, varying from zero to five, are possible. The dashed curve from a to b in figure 31 corresponds to a curve of symmetry-breaking bifurcation points of an unstable flow pattern denoted as B_8 in Puigjaner (2005). Hence, the B_3 solution manifold connects to the B_8 solution surface through this bifurcation curve. The other five curves in figure 31 are fold curves, i.e., curves formed by the loci of turning points. The cusp points labelled f, g and h in figure 31 correspond to codimension–two hysteresis points where two fold lines coalesce.

The bifurcation curves where the stability character of the B_3 solution changes are depicted as black solid lines over the solution surface in figure 30. This figure shows two different regions of stability, which correspond to the ranges $Pr^{-1} \leqslant 1.16$ ($Pr \geqslant 0.86$) and $Pr^{-1} \geqslant 1.24$ ($Pr \leqslant 0.81$), respectively. In the latter region the B_3 flow pattern becomes stable at considerably large values of Ra ($Ra \geqslant 90\,200$), but once it has become stable it remains so thereafter within the studied domain ($Ra \leqslant 1.5 \times 10^5$). On the contrary, in the region $Pr^{-1} \leqslant 1.16$ ($Pr \geqslant 0.86$) the B_3 flow pattern becomes stable at rather low values of Ra. These Ra values increase smoothly from Ra=20 600 to Ra=35 000, but the B_3 flow pattern becomes unstable at $Ra \leqslant 114\,700$, depending on Pr. Actually, the B_3 flow pattern becomes unstable as a consequence of a symmetry-breaking bifurcation that occurs at values of Ra within the range $79\,360 \leqslant Ra \leqslant 88\,050$ whenever Pr^{-1} is lower than 0.73 ($Pr > 1.73$). In the narrow region $0.73 \leqslant Pr^{-1} \leqslant 0.75$ ($1.33 \leqslant Pr \leqslant 1.37$) the B_3 flow pattern becomes unstable at the turning point over the fold line f-e in figure 31. Hence, the Rayleigh number where the B_3 flow pattern becomes unstable increase rapidly from Ra=88 050 to Ra=114 700 within this region. Finally, in the region $0.75 \leqslant Pr^{-1} \leqslant 1.16$ ($0.86 \leqslant Pr \leqslant 1.33$) the value of Ra where the B_3 flow pattern becomes unstable decreases smoothly from Ra=114 700 to Ra=35 000 and the instability is again due to a symmetry-breaking bifurcation.

In addition, there is a third small region of stability which can not be properly seen in figure 30. This region is the quasi triangular region α-δ-f in figure 32(a). Note that the point f corresponds to the cusp point depicted in figure 31. Two realisations of the B_3 flow pattern are simultaneously stable for values of Ra and Pr^{-1} within the region α-γ-β-f in figure 32(a). Accordingly, the tracked continuation solution curves plotted in figure 32(b) show that both curves corresponding to $Ra = 8.6 \times 10^4$ and $Ra = 9 \times 10^4$, respectively, present two stable realisations of the flow pattern at those values of Pr^{-1} within the region α-γ-β-f. On the other hand, as the value $Ra = 8.5 \times 10^4$ is outside the region α-γ-β-f, the corresponding curve in figure 32(b) presents only one stable realisation of the flow pattern. It is worth to note that the B_3 flow pattern is unstable in the whole Ra range investigated for $1.16 \leqslant Pr^{-1} \leqslant 1.24$ ($0.81 \leqslant Pr \leqslant 0.86$).

The development of the folds in the solution manifold near the cusp points g and h are shown in figure 33. The curves plotted in this figure were obtained by a sequence of continuation runs using Pr^{-1} as a continuation parameter at three values of Ra, namely 103×10^3, 104×10^3 and 105×10^3. It is clear that a saddle-like behaviour appears for Ra between 103×10^3 and 104×10^3. Figure 33 shows that five possible realisations of the B_3 flow pattern are possible for some values of Pr^{-1} at Ra=103×10^3 and Ra=104×10^3, in agreement with the parameter chart plotted in figure 31,

4. Conclusions

The bifurcation diagrams of steady flow patterns that develop inside a cubical cavity heated from below and filled either with air (Pr=0.71) or silicone oil (Pr=130) were determined by means of an arclength continuation procedure based on a Galerkin spectral method. The study was performed in the range $Ra \leqslant 1.5 \times 10^5$ and the four lateral walls were assumed to be perfectly conducting. Twenty-one and thirty-five solution branches were continued using Ra as parameter at Pr=0.71 and Pr=130, respectively. The stability analyses predicted that four (B_1, B_{11}, B_3, B_{312}) and nine steady flow patterns (B_1, B_2, B_{24}, B_{25}, B_{251}, B_{26}, B_3, B_{34}, B_5) were respectively stable at Pr=0.71 and 130 over certain ranges of Ra in the region investigated. The spatial configurations of the flow patterns are very similar to those developed for adiabatic lateral walls at values of Ra close to the bifurcation point where they set in but they become increasingly different as the Rayleigh number is increased. The higher complexity of the present problem, compared to the case with adiabatic lateral walls, is a direct consequence of the thermal activity of the lateral walls.

The comparison of the bifurcation diagrams at Pr=0.71 and 130 shows that the evolution of the flow patterns and their stability are strongly dependent on the Prandtl number. The flow patterns tend to adopt a double toroidal spatial configuration, even at moderate values of Ra when the cavity is filled with silicone oil (Pr=130). This double toroidal configuration consists of two torus-like vortices that respectively span most of the top and bottom halves of the cavity. As the sidewalls are thermally active, relatively warm fluid leaving the top plate boundary layer cools while dropping along the vertical walls. Similarly, the vertical walls warm fluid raising from the bottom plate boundary layer. Thus, the thermal activity of the sidewalls is the reason why almost every flow pattern, especially at Pr=130, tends to adopt the double toroidal topology as the Rayleigh number increases. The variation of the heat transfer rate at the bottom plate as a function of the two control parameters Ra and Pr^{-1} for the studied flow pattern B_3 yielded a rather complex three dimensional manifold that presented several folds and cusp points. The presence of folds in the solution manifold reveal that up to five realisations of the B_3 flow pattern are possible over some ranges of the parameters Ra and Pr^{-1} and that even two stable realisations coexist over a narrow region of the parameters. This explains the important differences in the spatial configuration and in the stability character of the B_3 flow pattern at different Prandtl numbers.

Present results are in fairly good agreement with the experimental results reported by Leong *et al.* (1999) at Pr=0.71 and Pallarès *et al.* (2001) at Pr=130. Current analysis provides a possible interpretation for the two different values of the heat transfer at the bottom plate, Nu_h, reported by Leong *et al.* (1999) at $Ra = 10^5$, and explains most of the experimental flow transitions between different steady flow patterns observed by Pallarès *et al.* (2001) over the region $Ra \leqslant 8 \times 10^4$.

Acknowledgements

The authors D. P., J. H. and F. G. are grateful for the financial support received from DGICYT project FIS2005-07194 and from the CIRIT "Programa de Grups de Recerca Consolidats de la Generalitat de Catalunya", project 2005SGR-00735. F. G. acknowledges the support received from the *Distinció a la Recerca de la Generalitat de Catalunya*. C. S. has been supported by grants DGICYT BFM2003-09504-C02-01, MTM2006-05849/Consolider (Spain) and CIRIT 2005SGR-1028 (Catalonia).

REFERENCES

Ahlers, G. 2000 Effect of sidewall conductance on heat–transport measurements for turbulent rayleigh–bénard convection. *Physical Review E* **63**, 015303.

Bodenschatz, E., Pesch, W. & Ahlers, G. 2000 Recent developments in rayleigh-bénard convection. *Annu. Rev. Fluid Mech.* **32**, 709–778.

Catton, I. 1970 Convection in a closed rectangular region: the onset of motion. *Transactions of the ASME* pp. 186–188.

Catton, I. 1972 The effect of insulating vertical walls on the onset of motion in a fluid heated from below. *Int. J. Heat Mass Transfer* **15**, 665–672.

Davis, S. H. 1967 Convection in a box: linear theory. *J. Fluid Mech.* **30**, 465–478.

Gelfgat, A. Y. 1999 Different modes of rayleigh–bénard instability in two and three dimensional rectangular enclosures. *J. Comput. Physics* **156**, 300–324.

Getling, A. V. 1998 *Rayleigh-Bénard convection: structures and dynamics*, *Advanced Series in Nonlinear Dynamics*, vol. 11. World Scientific Publishing.

Harris, L. & Reid, W. H. 1959 Critical rayleigh numbers for natural convection of water confined in square cells with l/d from 0.5 to 8. *ASME J. Heat Transfer* **93**, 188–196.

Jeong, J. & Hussain, F. 1995 On the identification of a vortex. *J. Fluid Mech.* **285**, 69–94.

Kessler, R. 1987 Nonlinear transition in three–dimensional convection. *J. Fluid Mech.* **174**, 357–379.

Koschmieder, E. L. 1993 *Bénard Cells and Taylor Vortices*. Cambridge: Cambridge University Press.

Lehoucq, R. B. & Sorensen, D. C. 1996 Deflation techniques for an implicitly restarted arnoldi iterations. *SIAM J. Matrix Anal. Appl.* **17**, 789.

Leong, W., Hollands, K. & Brunger, A. 1998 On a physically–realizable benchmark problem in internal natural convection. *Int. J. Heat Mass Transfer* **41**, 3817–3828.

Leong, W., Hollands, K. & Brunger, A. 1999 Experimental nusselt numbers for a cubical-cavity benchmark problem in natural convection. *Int. J. Heat Mass Transfer* **42**, 1979–1989.

Mizushima, J. & Matsuda, O. 1997 Onset of 3d thermal convection in a cubic cavity. *Journal of the Physical Society of Japan* **66**, 2237–2341.

Mizushima, J. & Nakamura, T. 2003 Onset of three–dimensional thermal convection in a rectangular parallelepiped cavity. *Journal of the Physical Society of Japan* **72**, 197–200.

Morgan, R. B. 1996 On restarting the arnoldi method for large nonsymmetric eigenvalue problems. *Mathematics of Computation* **65**, 1213–1230.

Pallarès, J., Arroyo, M., Grau, F. X. & Giralt, F. 2001 Experimental laminar rayleigh-bénard convection in a cubical cavity at moderate rayleigh and prandtl numbers. *Experiments in Fluids* **31**, 208–218.

Pepper, D. W. & Hollands, K. G. T. 2002 Summary of benchmark numerical studies for 3-d natural convection in an air–filled enclosure. *Numerical Heat Transfer. Part A* **42**, 1–11.

Puigjaner, D. 2005 Study of a natural convection problem inside a cubical cavity from the point of view of dynamical systems. PhD thesis, Facultat de Matemàtiques, Universitat de Barcelona, Barcelona. Spain.

Puigjaner, D., Herrero, J., Giralt, F. & Simó, C. 2004 Stability analysis of the flow in a cubical cavity heated from below. *Phys. Fluids* **16**, 3639–3655.

Puigjaner, D., Herrero, J., Giralt, F. & Simó, C. 2006 Bifurcation analysis of multiple steady flow patterns for rayleigh–bénard convection in a cubical cavity at $pr = 130$. *Physical Review E* **73**, 046304.

Roche, P. E., Castaing, B., Chabaud, B., Hébral, B. & Sommeria, J. 2001 Side wall effects in rayleigh-bénard experiments. *Eur. Phys. J. B* **24**, 405–408.

$Ra/10^3$	Nu	$\Delta(\%)$	$Ra/10^3$	Nu	$\Delta(\%)$	Flow pattern
44	2.047	0.4	150	2.423	1.4	B_1
91	3.999	2.8	150	5.079	3.3	B_3
45	2.103	0.3	150	4.582	2.0	B_{11}
25	1.617	0.2	87	3.221	2.3	B_{312}

TABLE 1. Nusselt numbers calculated by the Galerkin continuation method at Pr=0.71 and the relative differences with respect the Nusselt number obtained by the finite-difference solver. Only those flow patterns that are stable over certain ranges within the studied domain (see §3.1) are listed.

SÁNCHEZ, J., NET, M., GARCÍA-ARCHILLA, B. & SIMÓ, C. 2004 Newton-krylov continuation of periodic orbits for navier-stokes flows. *J. of Computational Physics* **201**, 13–33.

SIMÓ, C. 1990 Analytical and numerical computation of invariant manifolds. In *Modern methods in celestial mechanics* (ed. D. Benest & C. Froeschlé), pp. 285–330. Paris: Editions Frontières.

VERZICCO, R. 2002 Sidewall finite–conductivity effects in confined turbulent thermal convection. *J. Fluid Mech.* **473**, 201–203.

YANG, K. T. 1988 Transitions and bifurcations in laminar buoyant flows in confined enclosures. *ASME J. Heat Transfer* **110**, 1191–1204.

$Ra/10^3$	Nu	$\Delta(\%)$	$Ra/10^3$	Nu	$\Delta(\%)$	Flow pattern
57	2.963	1.2	150	4.689	2.9	B_1
80	3.120	1.1	150	4.241	2.3	B_2
79	3.402	2.1	150	4.484	2.9	B_3
95	3.750	1.7	150	4.546	2.5	B_5
67.72	2.822	0.6	112	3.461	1.5	B_{24}
86	3.245	1.2				B_{25}
113	3.727	2.0	150	4.234	2.3	B_{26}
80	3.425	1.8	94	3.732	3.1	B_{34}
90	3.301	1.3	150	4.212	2.2	B_{251}

Table 2. Nusselt numbers calculated by the Galerkin continuation method at Pr=130 and the relative differences with respect the Nusselt number obtained by the finite-difference solver. Only those solutions that are stable at certain ranges within the studied domain (see §3.1) are listed.

Catton (1970)	Mizushima and Matsuda (1997)	Leong et al. (1998)	Present work	Flow pattern
6 974	6 798	$6\,969 \pm 144$ $7\,058 \pm 119$	6 799	B_1 (x or y–roll)
–	8 437	–	8 353	B_4 (single toroid)
–	11 609	–	11 612	B_3 (four connected half–rolls)

Table 3. Comparison of primary bifurcation Rayleigh numbers reported in the literature (Catton 1970; Mizushima & Matsuda 1997; Leong *et al.* 1998) with present predictions. Since the values reported by Leong *et al.* (1998) are experimental, they include their corresponding 95% confidence limits of uncertainty.

Ra	Flow pattern	Generators of the symmetry group	Brief description
6 798	B_1	$S_y,\ -I$	y–roll
	B_2	$S_{d_-},\ -I$	diagonal roll
8 353	B_4	$S_x,\ S_y,\ S_{d_+}$	single toroid
11 612	B_3	$-S_y,\ S_{d_+},\ S_{d_-}$	four interconnected half–rolls
14 770	B_5	$S_x,\ S_y,\ -S_y \cdot S_{d_+}$	four interconnected half–rolls diagonally aligned
23 498	B_6	$S_y,\ -I$	six interconnected half–rolls
	B_7	$S_{d_-},\ -I$	three diagonal rolls
27 746	B_8	$S_x,\ S_y,\ S_z,\ S_{d_+}$	double toroid

Table 4. Primary bifurcation Rayleigh numbers obtained for $Ra < 3 \times 10^4$.

Flow pattern	Range of existence	Range of stability	Generators of the symmetry group	Topology shown in figures
B_1	6 798–	6 798–44 700	$S_y,\ -I$	6 and 7
B_{11}	44 700–	44 700–88 205	S_y	8
B_3	11 612–	90 210–	$S_{d_+},\ S_{d_-},\ -S_y$	9 and 10
B_{312}	22 575–87 481	22 575–70 683	$S_{d_+},\ S_{d_-}$	11 and 12

Table 5. Summary of the range of existence, the range of stability and the symmetry properties of those solutions that are stable over certain ranges of the Rayleigh number in the region $Ra < 1.5 \times 10^5$ at Pr=0.71. S_y, S_{d_+}, S_{d_-}, and $-I$ are matrix representations of elements of the groups of symmetries.

Flow pattern	Range of existence	Range of stability	Generators of the symmetry group	Topology shown in figures
B_1	6 798–	6 798–57 304	S_y, $-I$	15 and 16(a)
B_2	6 798–	67 730–85 694	S_{d_-}, $-I$	17
B_{24}	42 659–112 381	67 713–67 730	S_{d_-}	16(b)
B_{25}	85 694–87 598	85 694–87 598	$-I$	16(c)
B_{251}	48 116–	61 160–65 297 87 598–	S_y, $-I$	18 and 19
B_{26}	112 622–	146 738–	$-S_{d_-} = S_{d_+} S_z$	16(d)
B_3	11 612–	20 637–79 362	$-S_y$, S_{d_+}, S_{d_-}	21
B_{34}	79 362–94 417	79 362–94 417	$-S_y \cdot S_{d_+}$, $S_x \cdot S_y = -S_z$	23
B_5	14 770–	94 417–	S_x, S_y, $-S_y \cdot S_{d_+}$	20 and 22

Table 6. Summary of the range of existence, the range of stability and the symmetry properties of those solutions that are stable over certain ranges of the Rayleigh number in the region $Ra < 1.5 \times 10^5$ at Pr=130. S_y, S_{d_-}, S_{d_+}, $-S_y$ and S_x are matrix representations of elements of the groups of symmetries.

$Ra/10^3$	Nu		Flow pattern
	Present work	Leong et al. (1999)	
10	1.202	1.246 ± 0.013	B_1
40	2.008	2.018 ± 0.017	B_1
100	3.648	3.509 ± 0.035	B_{11}
100	4.062	3.916 ± 0.042	B_{11}

Table 7. Comparison of the cold plate Nusselt numbers with experimental results reported by Leong *et al.* (1999). The last column includes the corresponding flow pattern predicted in the current study.

Flow pattern	$Ra/10^3$	Pr	Nu_h	Nu_t	Nu_{ad}	F	C
B_1	50	0.71	2.13	3.27	3.07	0.35	−0.31
B_1	150	0.71	2.42	4.19	4.05	0.42	−0.40
B_1	50	130	2.74	3.62	3.10	0.24	−0.12
B_1	150	130	4.69	6.26	4.13	0.25	0.14
B_{11}	88	0.71	3.89	5.31	4.04	0.27	−0.04
			3.40			0.36	−0.16
B_{11}	150	0.71	4.58	6.18	5.10	0.26	−0.10
			4.37			0.29	−0.14
B_2	150	130	4.24	5.94	4.41	0.29	−0.04
B_3	150	0.71	5.08	7.43	5.41	0.32	−0.06
B_3	150	130	4.48	5.93	5.07	0.24	−0.12

TABLE 8. Comparison of present heat transfer coefficients, Nu_h and Nu_t with that obtained for adiabatic lateral walls, Nu_{ad}. The two possible Nu_h values, depending on the y-vorticity sign, are included for the B_{11} flow pattern. The two last columns include the relative factors $F = (Nu_t - Nu_h)/Nu_t$ and $C = (Nu_h - Nu_{ad})/Nu_{ad}$.

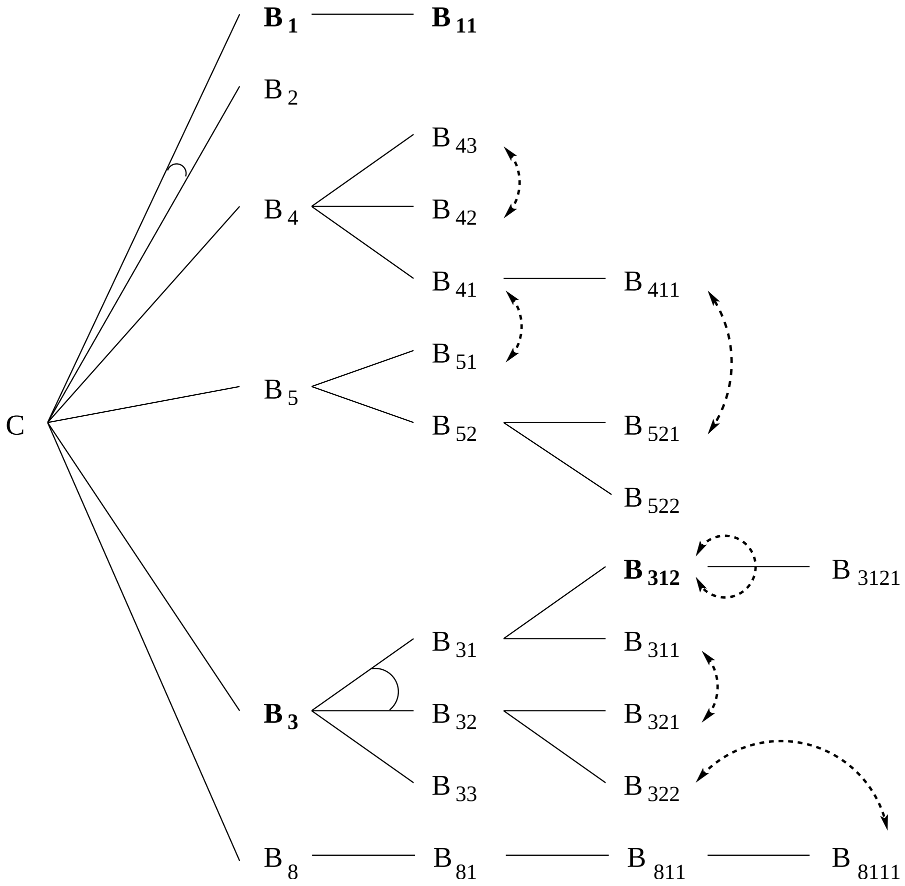

FIGURE 1. Sketch of the bifurcation diagram at Pr=0.71. Solutions that are connected by a dashed arrow represent the same flow pattern. Solutions that set in at the same bifurcation point are joined with a solid arc. Those flow patterns printed in boldface are stable over certain ranges of Rayleigh numbers in the region $Ra \leqslant 1.5 \times 10^5$.

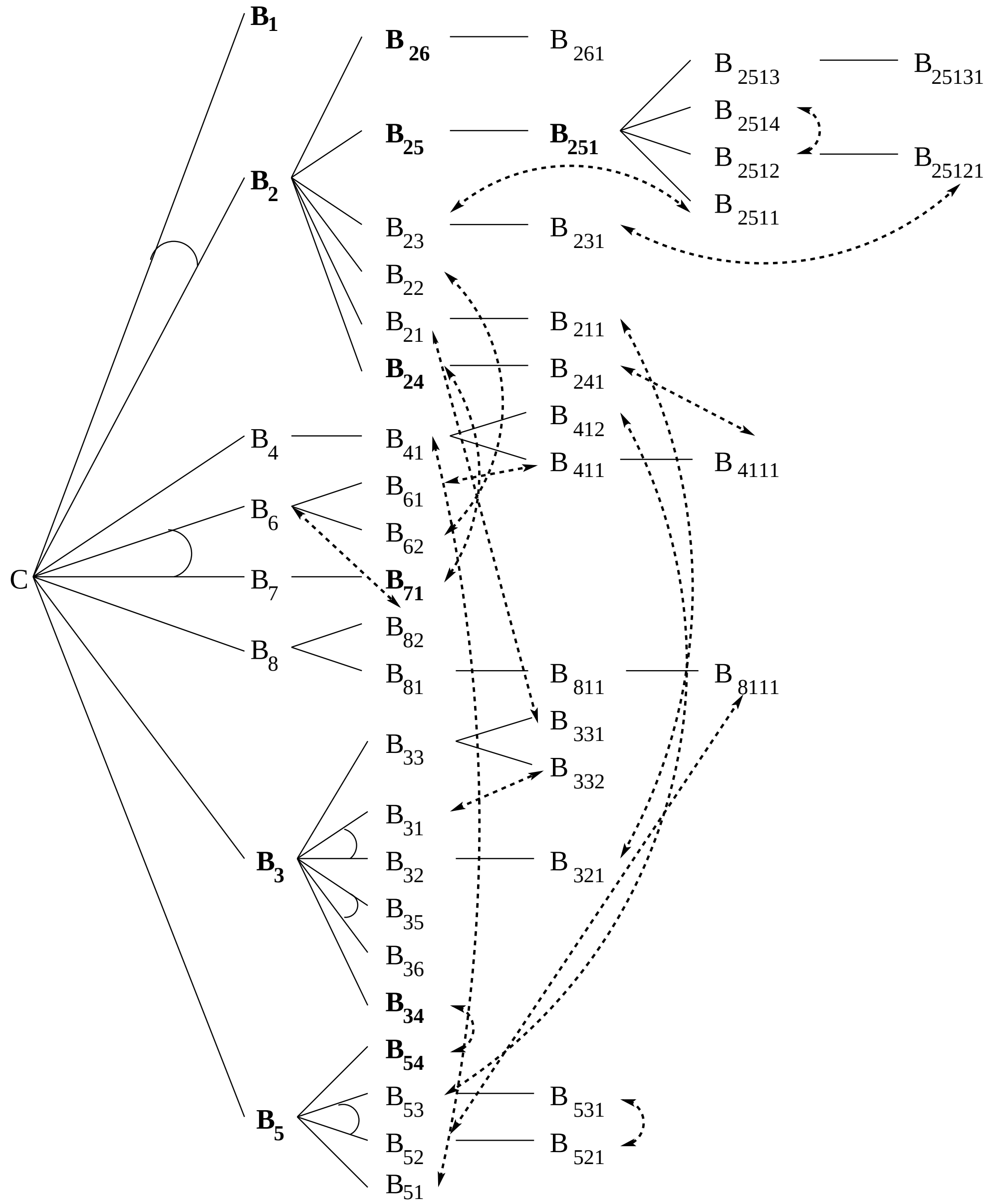

FIGURE 2. Sketch of the bifurcation diagram at Pr=130. Solutions that are connected by a dashed arrow represent the same flow pattern. Solutions that set in at the same bifurcation point are joined with a solid arc. Those flow patterns printed in boldface are stable over certain ranges of Rayleigh numbers in the region $Ra \leqslant 1.5 \times 10^5$.

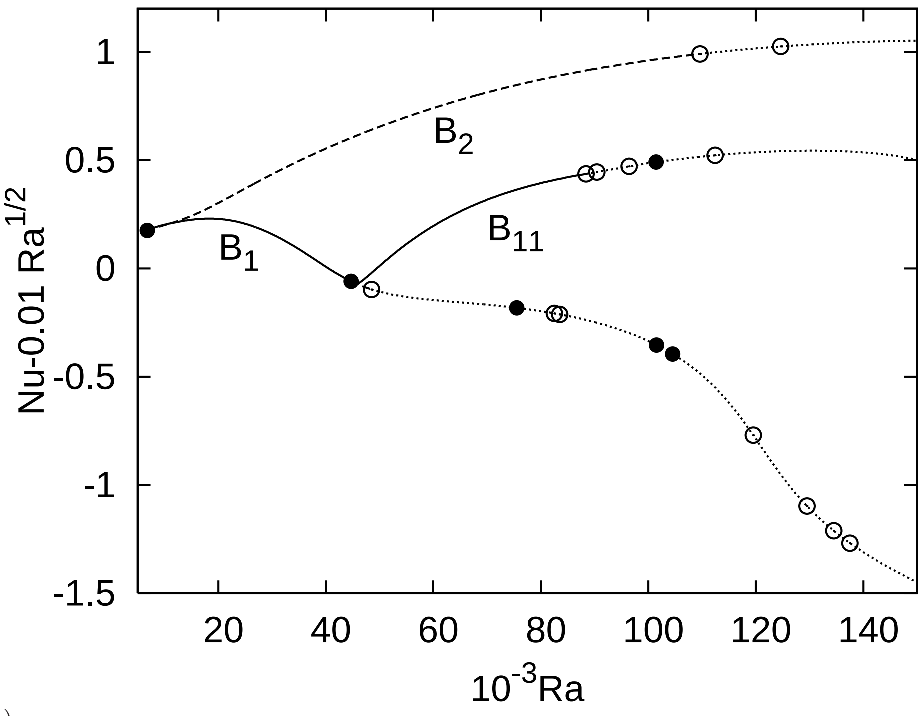

1
0.5
0
-0.5
-1
-1.5
20
40
60
80
100
120
140
$Nu\text{-}0.01\ Ra^{1/2}$
$10^{-3}Ra$
B_2
B_1
B_{11}

a)

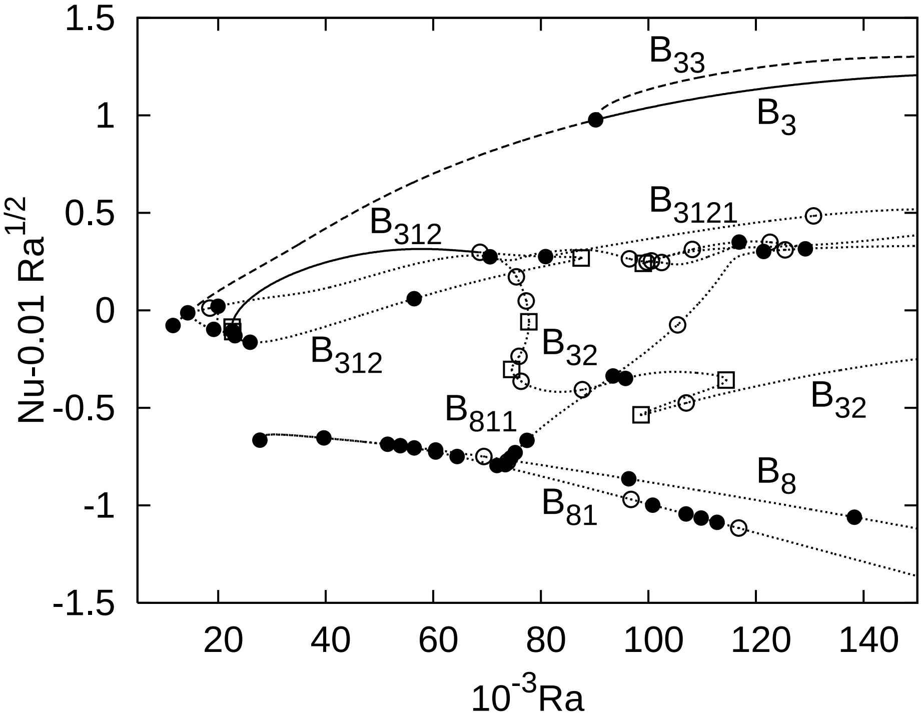

1.5
1
0.5
0
-0.5
-1
-1.5
20
40
60
80
100
120
140
$Nu\text{-}0.01\ Ra^{1/2}$
$10^{-3}Ra$
B_{33}
B_3
B_{3121}
B_{312}
B_{312}
B_{32}
B_{32}
B_{811}
B_8
B_{81}

b)

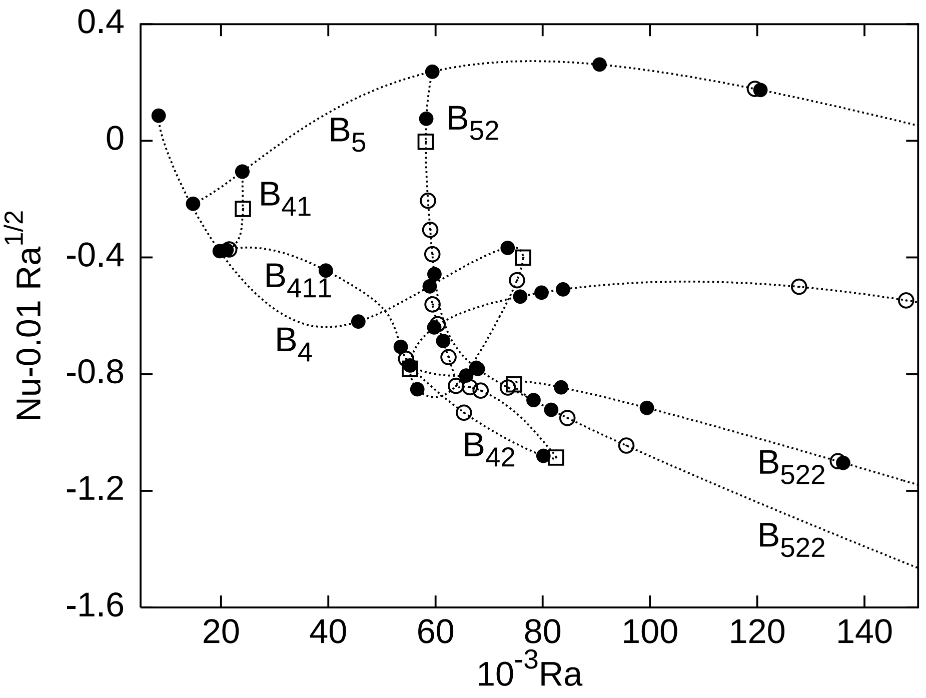

c)

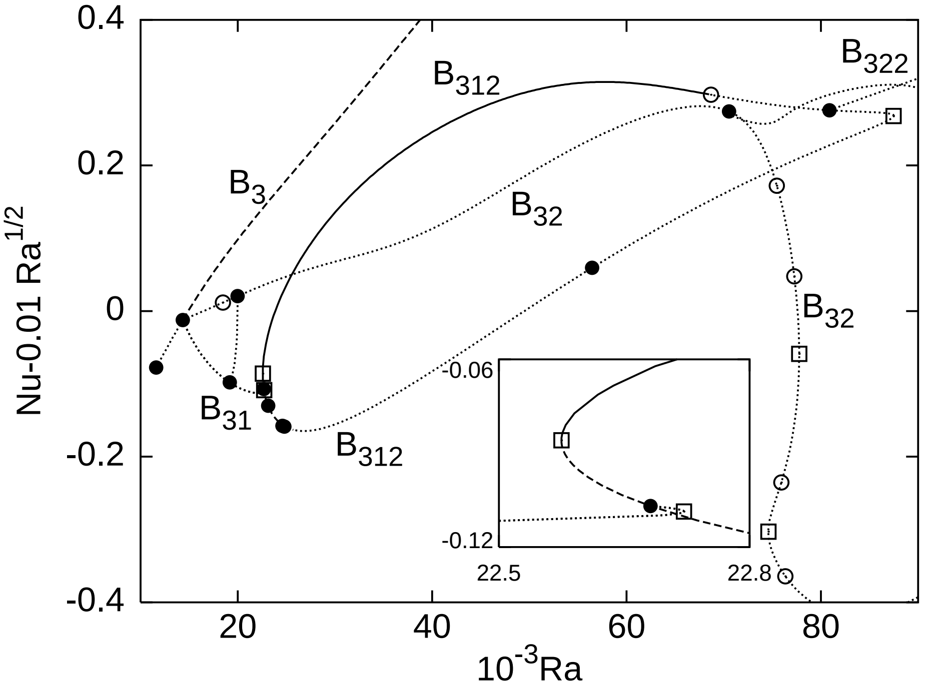

d)

FIGURE 3. (a-c) Bifurcation diagram at Pr=0.71. For the sake of clarity the bifurcation diagram is presented in three plots. (d) Zoom of the bifurcation diagram depicted in (b), which includes an additional zoom of a smaller domain. Stable flow patterns are depicted with solid lines. Unstable flow patterns are represented by dashed lines when they have exactly one unstable eigenmode and by dotted lines when they have two or more unstable eigenmodes. Steady bifurcations, Hopf bifurcations and turning points are represented by filled circles, hollow circles and hollow squares, respectively.

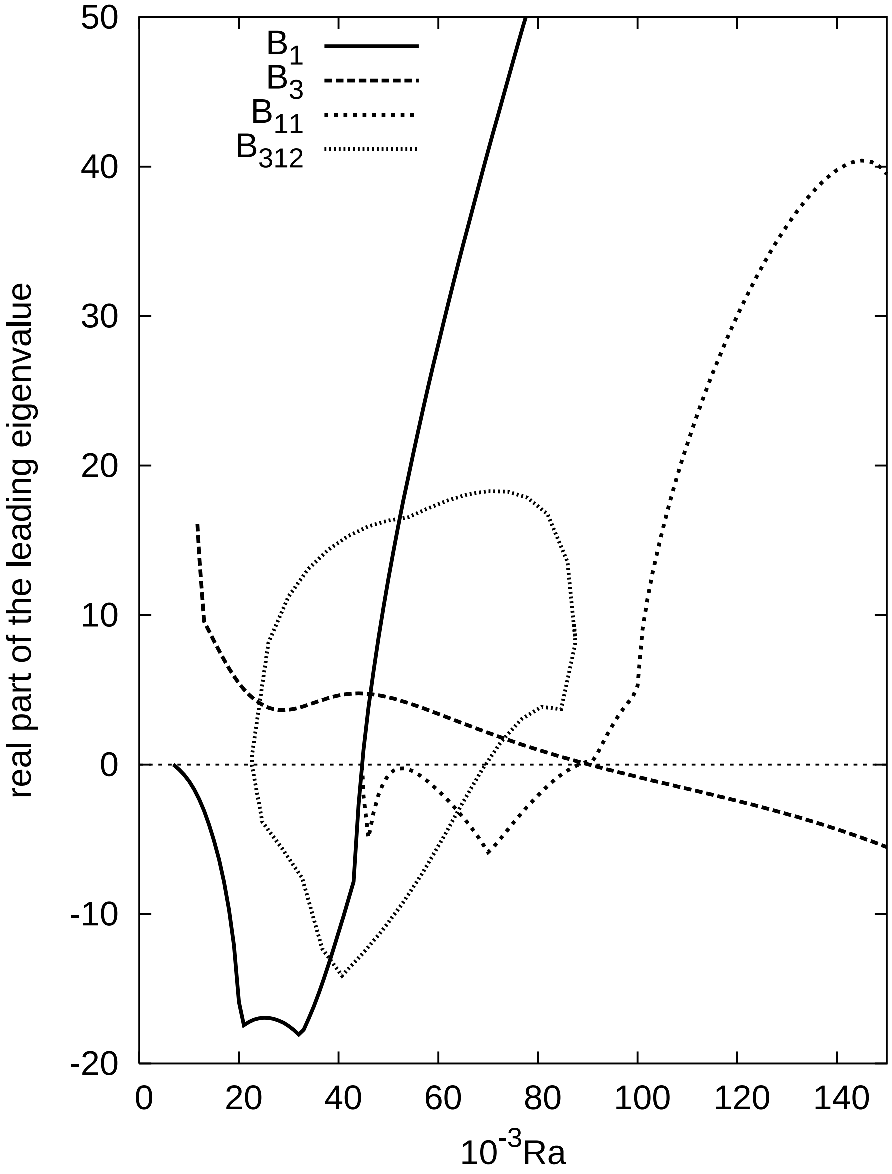

FIGURE 4. Variation of the real part of the leading eigenvalue with $10^{-3}Ra$ for those flow patterns that are stable over certain ranges in Ra at Pr=0.71.

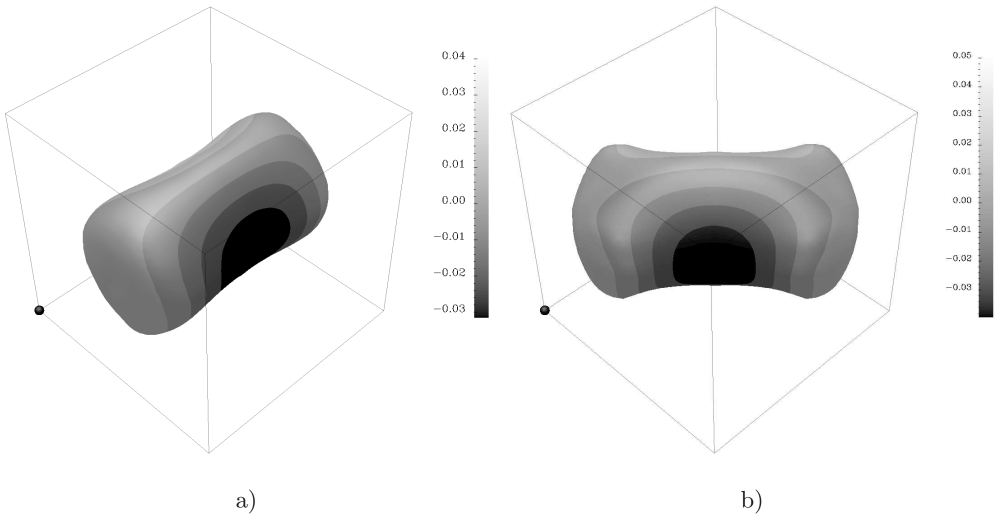

FIGURE 5. Surface of $\lambda_2 = 0$ for (a) the stable B_1 flow pattern and (b) the unstable B_2 flow pattern at $Ra = 7 \times 10^3$. The grey levels are scaled with the value of the vertical velocity component. Here and in all subsequent plots of surfaces of $\lambda_2 = 0$, the filled circle denotes the vertex with coordinates $(-0.5, -0.5, -0.5)$ while the coordinates of the lower frontal vertex are $(0.5, -0.5, -0.5)$.

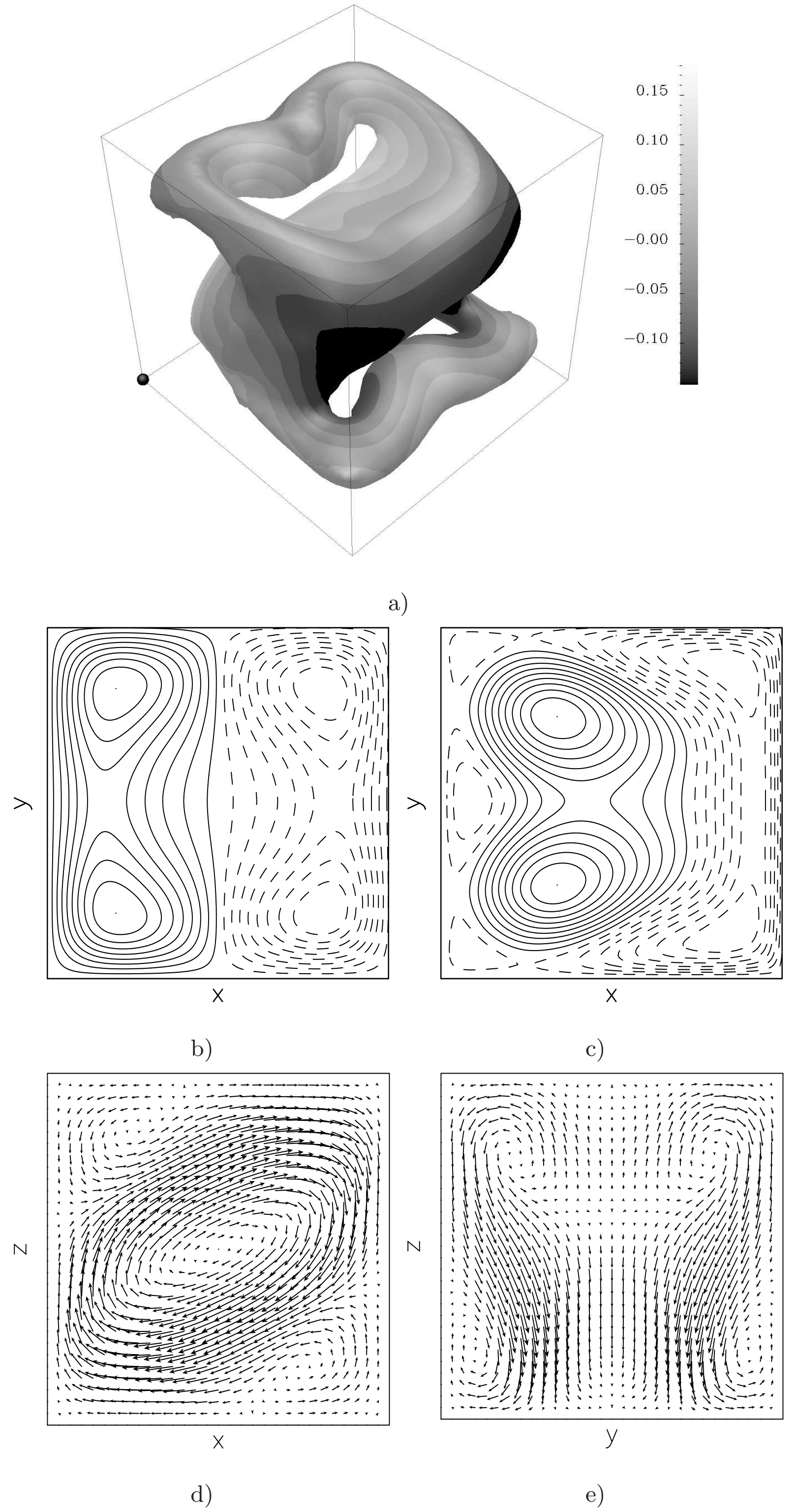

FIGURE 6. Stable B_1 flow pattern at $Ra = 4.4 \times 10^4$ and Pr=0.71. (a) Surface of $\lambda_2 = 0$. The grey levels are scaled with the value of the vertical velocity component. Vertical velocity contours at the horizontal planes (b) $z = 0$ and (c) $z = 0.25$. Positive and negative values of the velocity are plotted with solid and dashed lines, respectively. Projected velocity vectors at vertical planes (d) $y = 0$ and (e) $x = 0.125$.

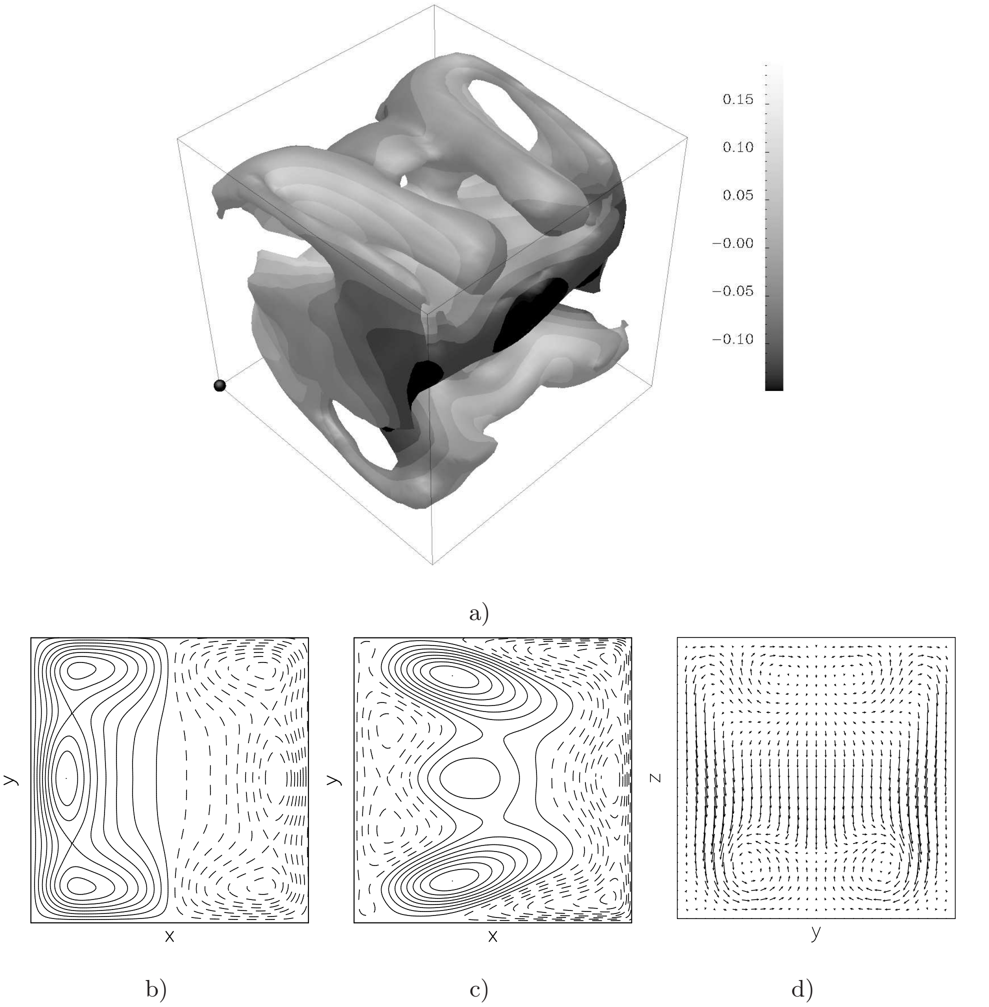

FIGURE 7. Unstable B_1 flow pattern at $Ra = 1.5 \times 10^5$ and Pr=0.71. (a) Surface of $\lambda_2 = 0$. The grey levels are scaled with the value of the vertical velocity component. Vertical velocity contours at the horizontal planes (b) $z = 0$ and (c) $z = 0.25$. Positive and negative values of the velocity are plotted with solid and dashed lines, respectively. (d) Projected velocity vectors at vertical plane $x = 0.125$.

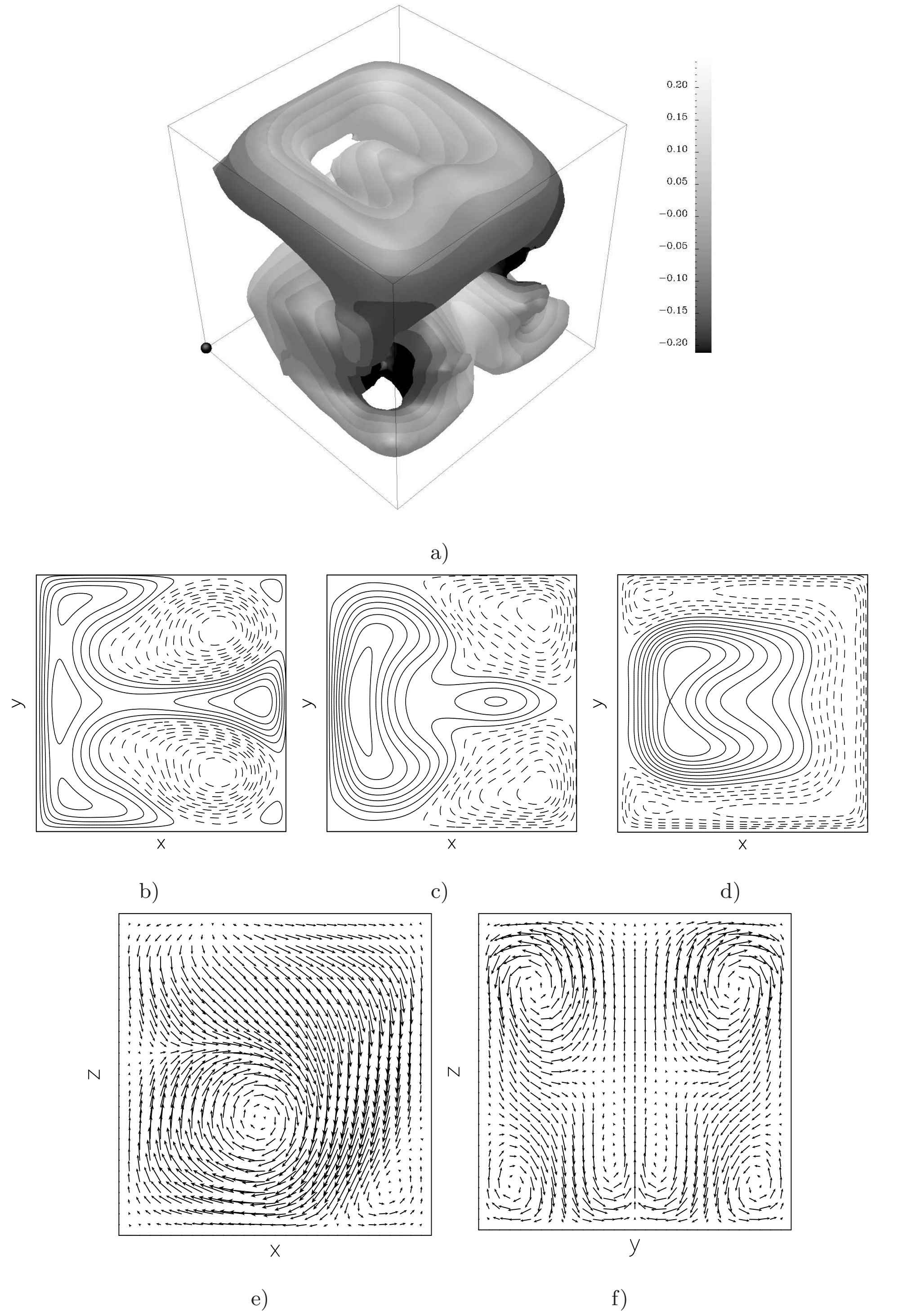

FIGURE 8. Stable B_{11} flow pattern at $Ra = 8.8 \times 10^4$ and Pr=0.71. (a) Surface of $\lambda_2 = 0$. The grey levels are scaled with the value of the vertical velocity component. Vertical velocity contours at the horizontal planes (b) $z = -0.25$, (c) $z = 0$ and (d) $z = 0.25$. Positive and negative values of the velocity are plotted with solid and dashed lines, respectively. Projected velocity vectors at vertical planes (e) $y = 0.375$ and (f) $x = 0$.

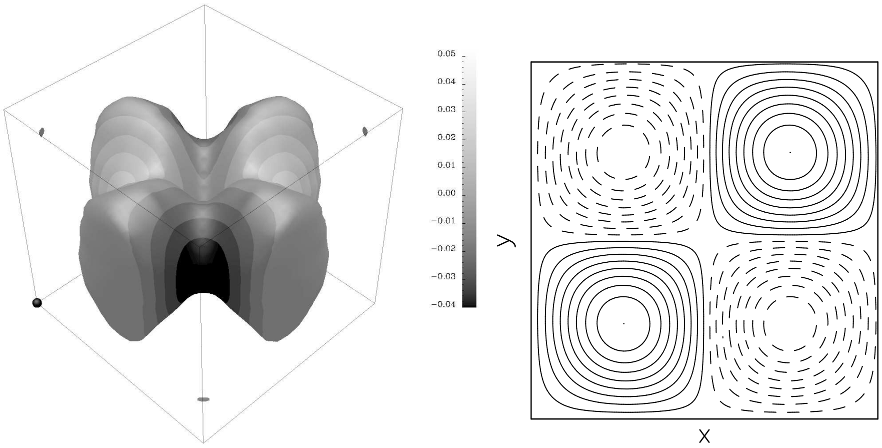

a) b)

FIGURE 9. Unstable B_3 flow pattern at $Ra = 1.2 \times 10^4$ and Pr=0.71. (a) Surface of $\lambda_2 = 0$. The grey levels are scaled with the value of the vertical velocity component. (b) Vertical velocity contours at the horizontal midplane $z = 0$. Positive and negative values of the velocity are plotted with solid and dashed lines, respectively.

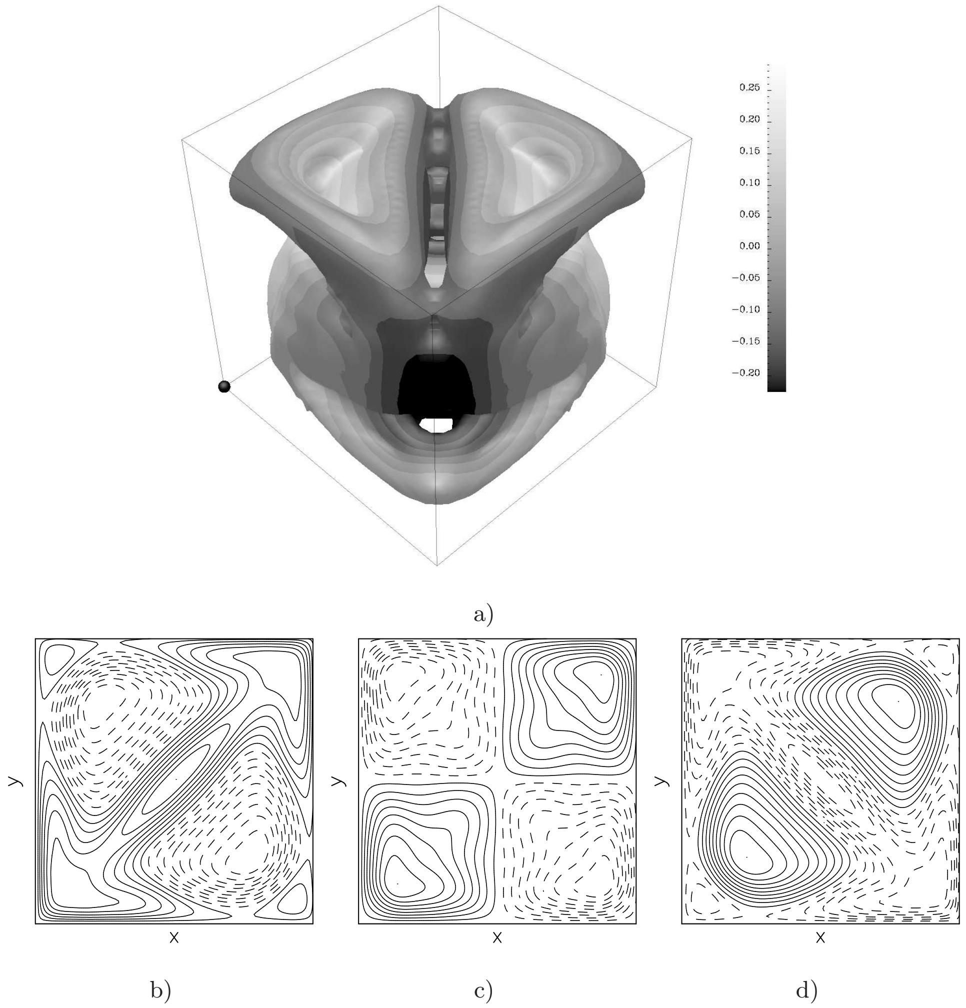

FIGURE 10. Stable B_3 flow pattern at $Ra = 1.5 \times 10^5$ and Pr=0.71. (a) Surface of $\lambda_2 = 0$. The grey levels are scaled with the value of the vertical velocity component. Vertical velocity contours at the horizontal planes (b) $z = -0.25$, (c) $z = 0$ and (d) $z = 0.25$. Positive and negative values of the velocity are plotted with solid and dashed lines, respectively.

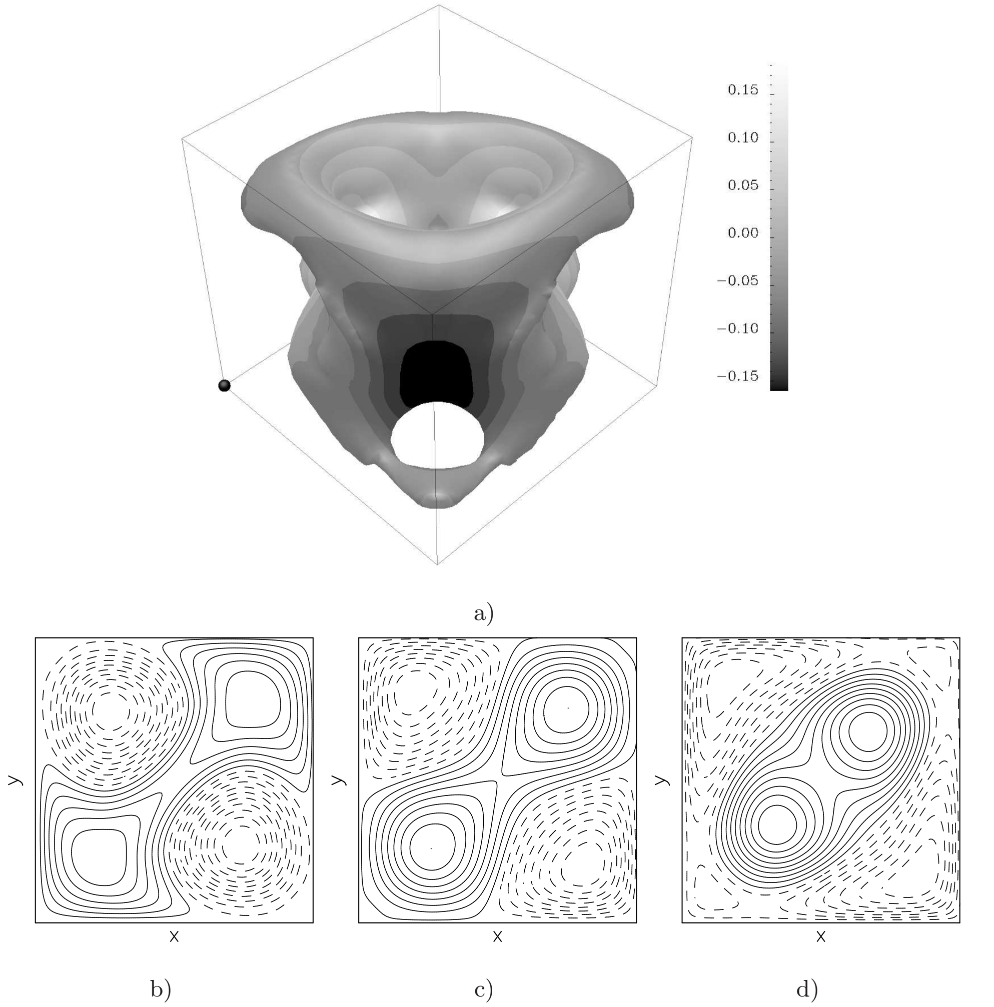

FIGURE 11. Stable B_{312} flow pattern at $Ra = 2.5 \times 10^4$ and Pr=0.71. (a) Surface of $\lambda_2 = 0$. The grey levels are scaled with the value of the vertical velocity component. Vertical velocity contours at the horizontal planes (b) $z = -0.25$, (c) $z = 0$ and (d) $z = 0.25$. Positive and negative values of the velocity are plotted with solid and dashed lines, respectively.

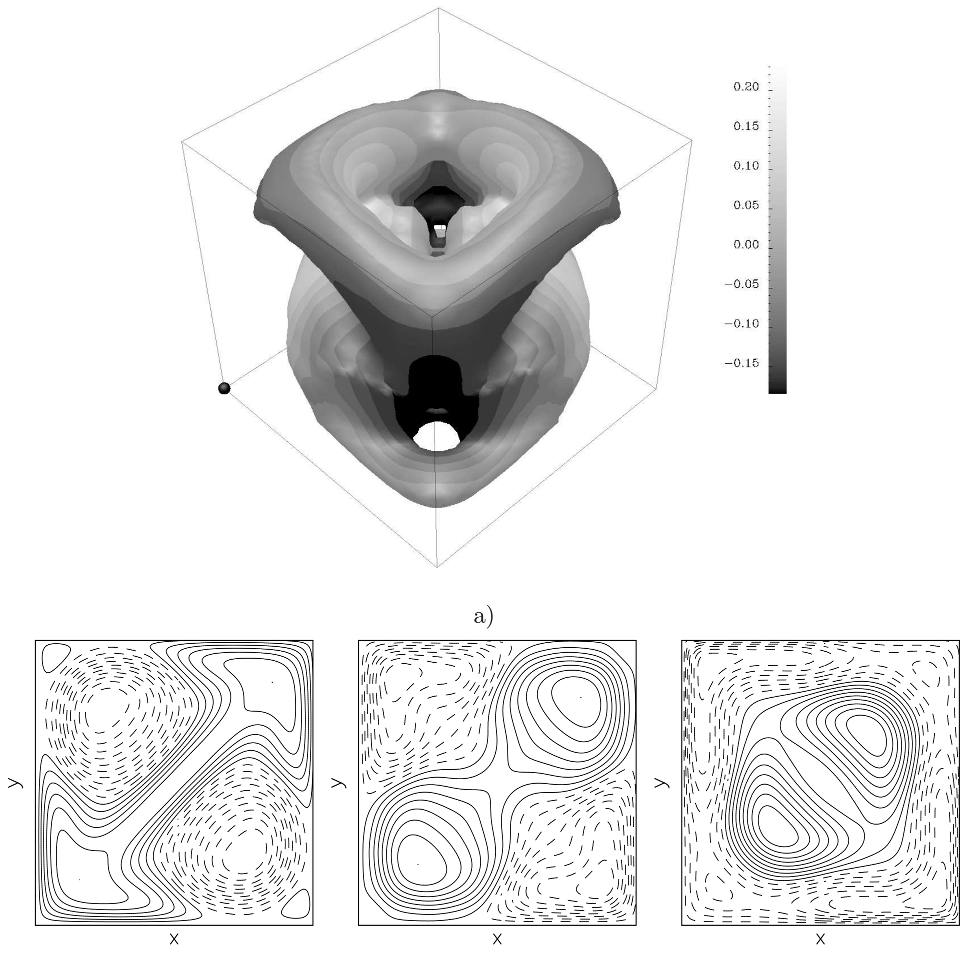

a)

b) c) d)

FIGURE 12. Stable B_{312} flow pattern at $Ra = 8.7 \times 10^4$ and Pr=0.71. (a) Surface of $\lambda_2 = 0$. The grey levels are scaled with the value of the vertical velocity component. Vertical velocity contours at the horizontal planes (b) $z = -0.25$, (c) $z = 0$ and (d) $z = 0.25$. Positive and negative values of the velocity are plotted with solid and dashed lines, respectively.

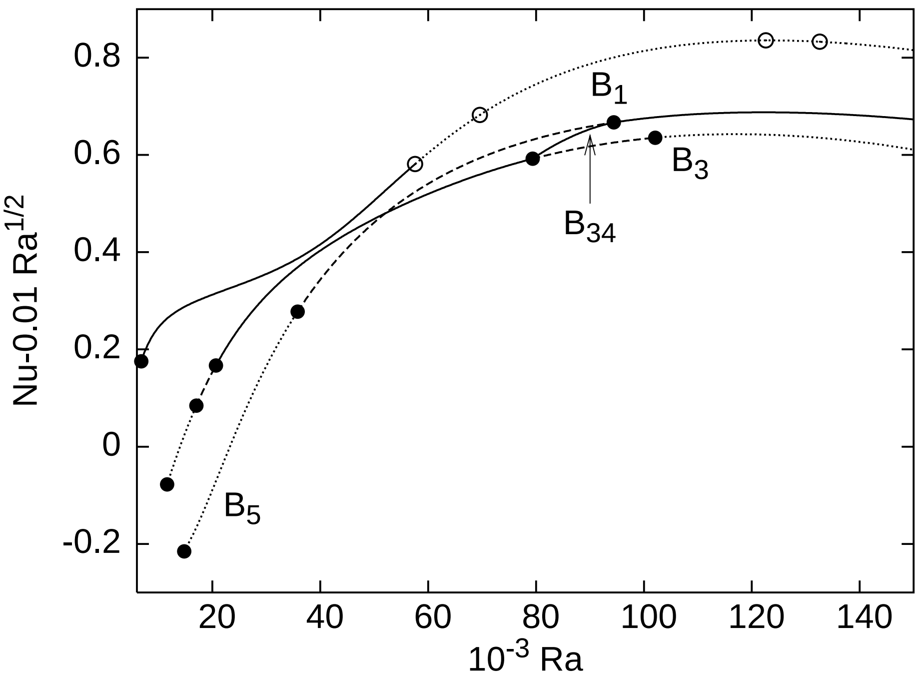
0.8
0.6
0.4
0.2
0
-0.2
Nu-0.01 Ra^1/2
20
40
60
80
100
120
140
10^-3 Ra
B1
B3
B34
B5

a)

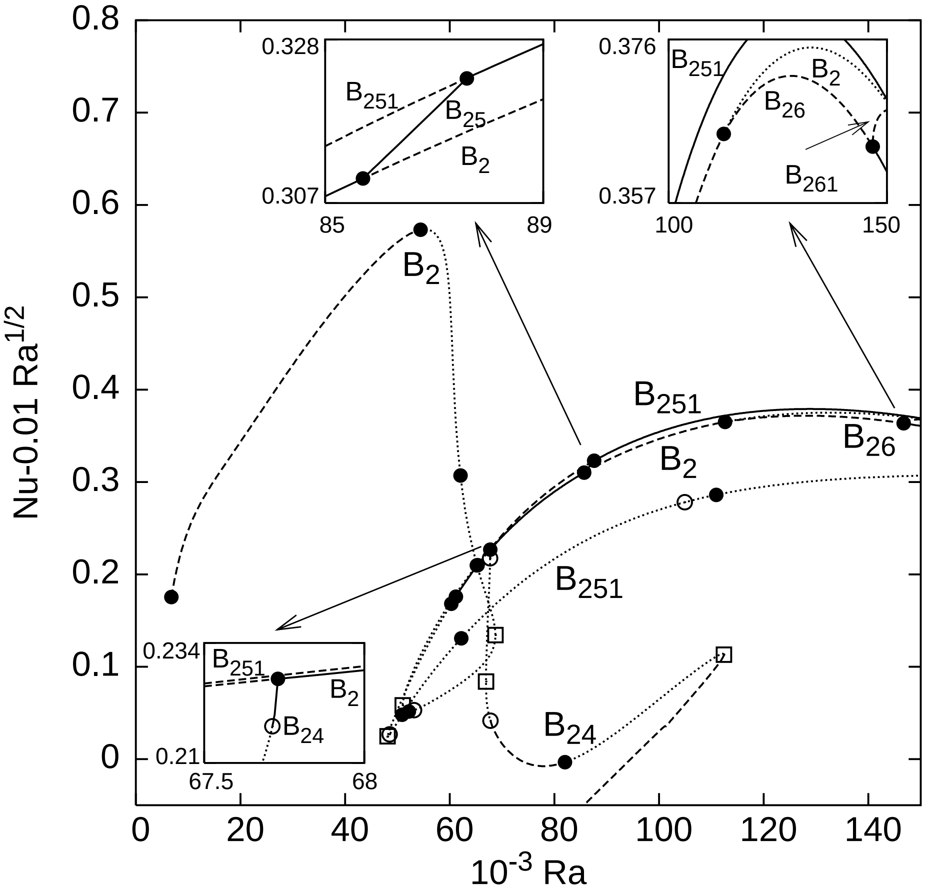

b)

FIGURE 13. (a,b) Bifurcation diagram at Pr=130. For the sake of clarity the bifurcation diagram is presented in two plots. Stable flow patterns are depicted with solid lines. Unstable flow patterns are represented by dashed lines when they have exactly one unstable eigenmode and by dotted lines when they have two or more unstable eigenmodes. Steady bifurcations, Hopf bifurcations and turning points are represented by filled circles, hollow circles and hollow squares, respectively. Additional zooms of smaller domains are included.

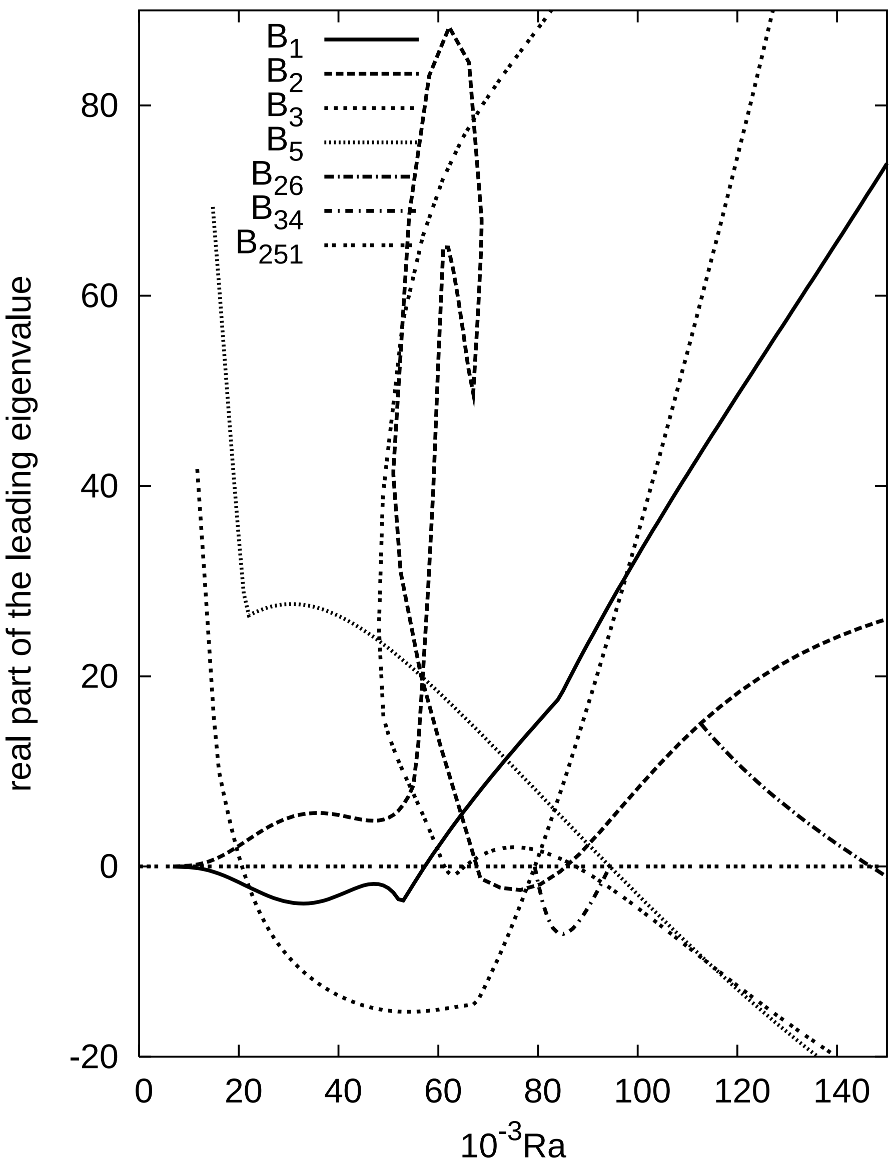

FIGURE 14. Variation of the real part of the leading eigenvalue with $10^{-3}Ra$ for those flow patterns that are stable over certain ranges in Ra at Pr=130.

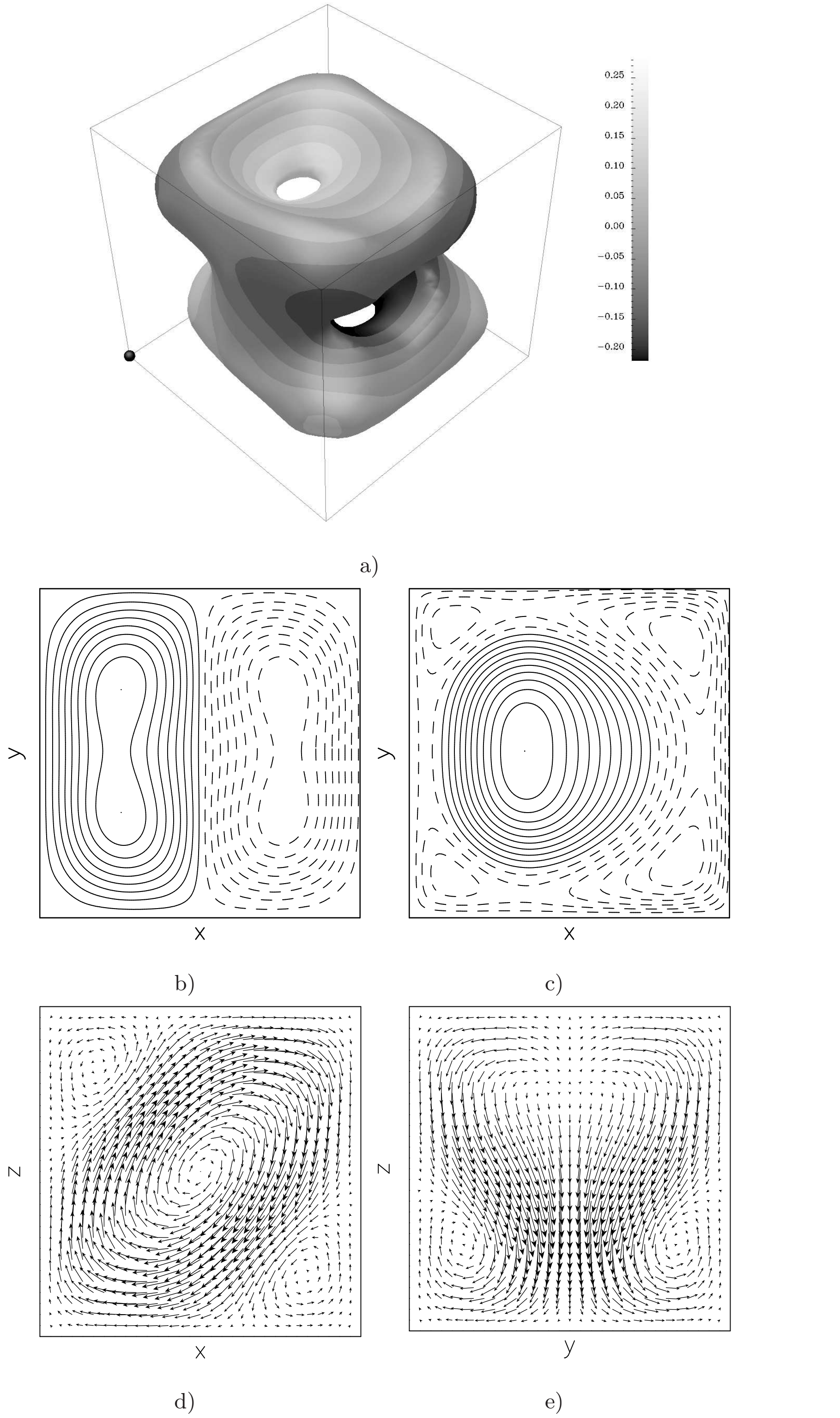

FIGURE 15. Stable B_1 flow pattern at $Ra = 5 \times 10^4$ and Pr=130. (a) Surface of $\lambda_2 = 0$. The grey levels are scaled with the value of the vertical velocity component. Vertical velocity contours at the horizontal planes (b) $z = -0.25$, (c) $z = 0$ and (d) $z = 0.25$. Positive and negative values of the velocity are plotted with solid and dashed lines, respectively. Projected velocity vectors at vertical planes (d) $y = 0.25$ and (e) $x = 0.25$.

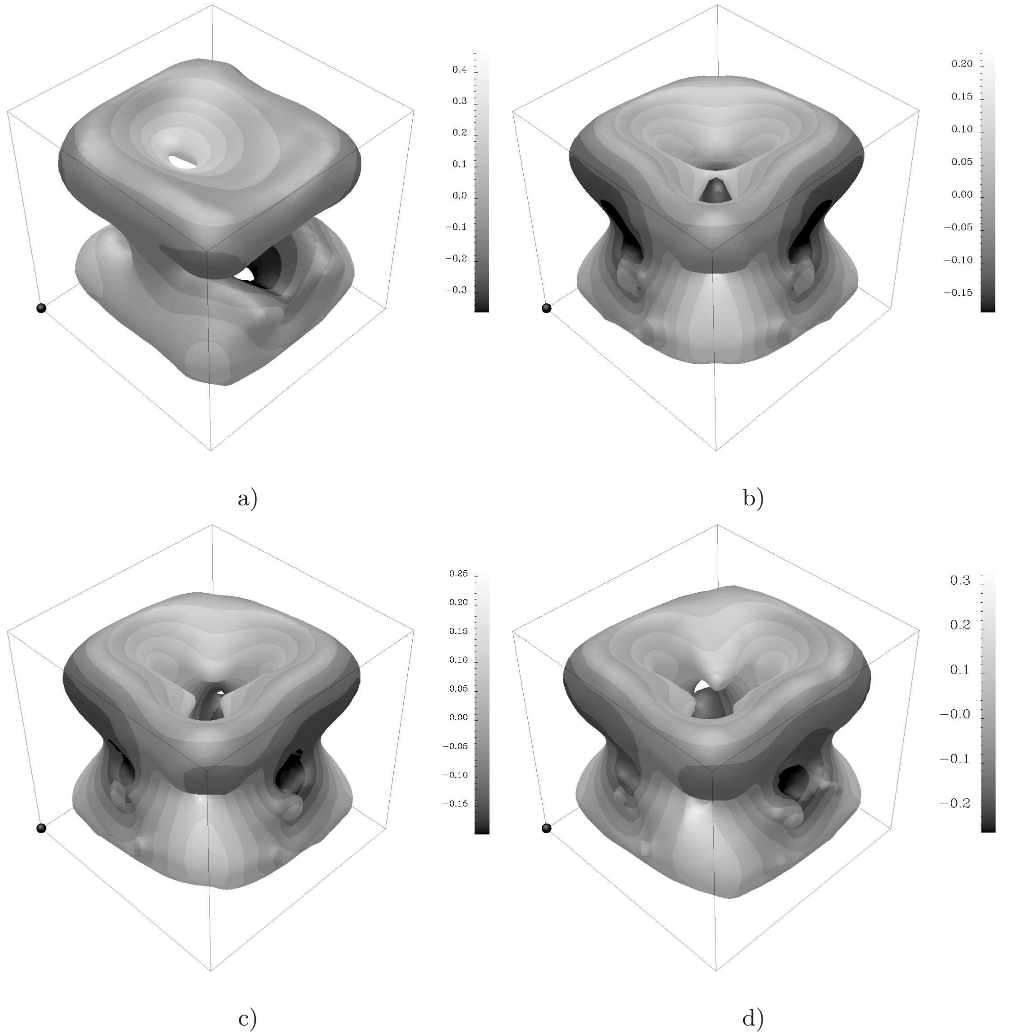

FIGURE 16. Surfaces of $\lambda_2 = 0$ at Pr=130. a) Unstable B_1 flow pattern at $Ra = 1.5 \times 10^5$. b) Stable B_{24} flow pattern at $Ra = 67\,720$. c) Stable B_{25} flow pattern at $Ra = 86\,000$. d) Stable B_{26} flow pattern at $Ra = 1.5 \times 10^5$. The grey levels are scaled with the value of the vertical velocity component.

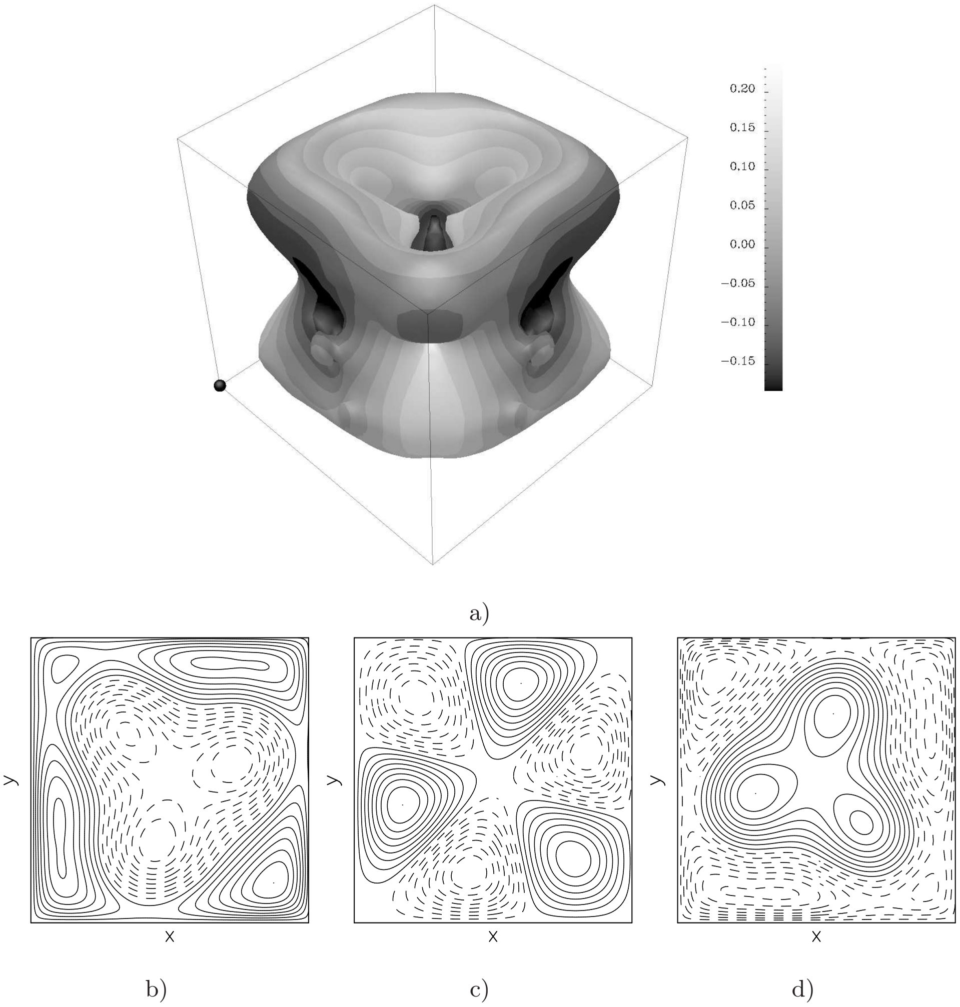

FIGURE 17. Stable B_2 flow pattern at $Ra = 8 \times 10^4$ and Pr=130. (a) Surface of $\lambda_2 = 0$. The grey levels are scaled with the value of the vertical velocity component. Vertical velocity contours at the horizontal planes (b) $z = -0.25$, (c) $z = 0$ and (d) $z = 0.25$. Positive and negative values of the velocity are plotted with solid and dashed lines, respectively.

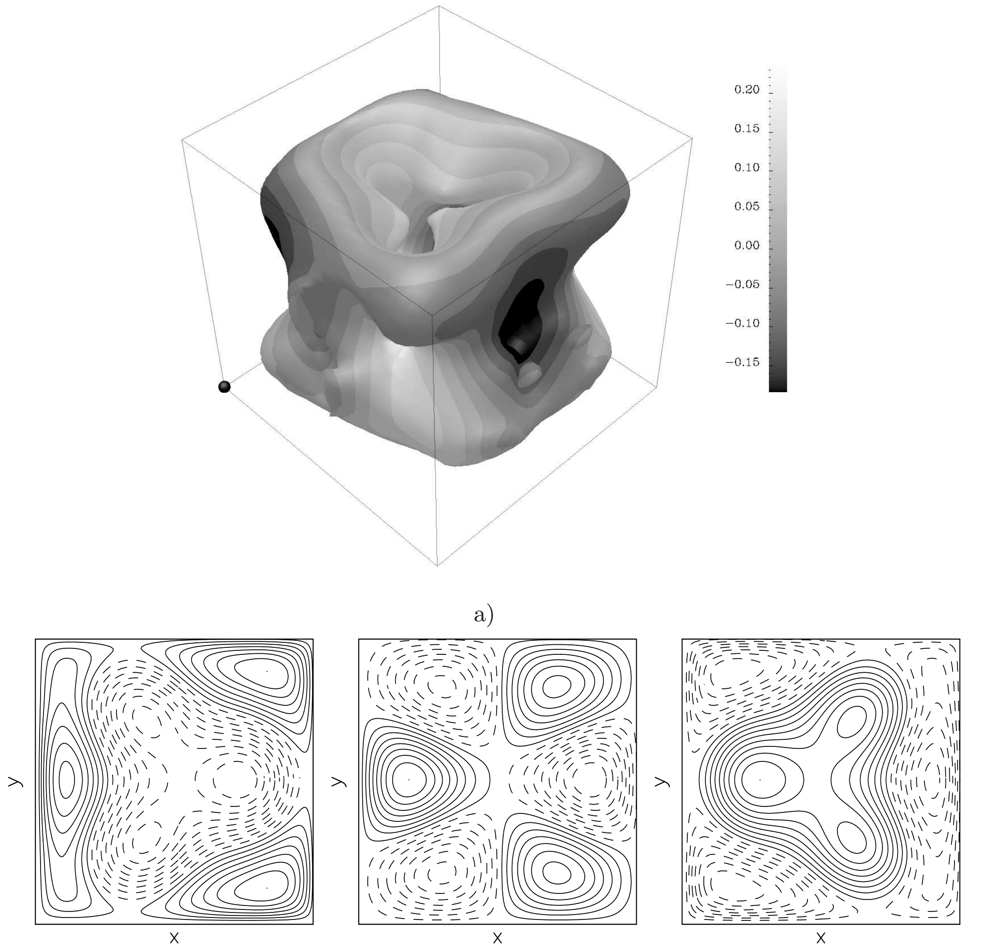

b) c) d)

FIGURE 18. Stable B_{251} flow pattern at $Ra = 6.3 \times 10^4$ and Pr=130. (a) Surface of $\lambda_2 = 0$. The grey levels are scaled with the value of the vertical velocity component. Vertical velocity contours at the horizontal planes (b) $z = -0.25$, (c) $z = 0$ and (d) $z = 0.25$. Positive and negative values of the velocity are plotted with solid and dashed lines, respectively.

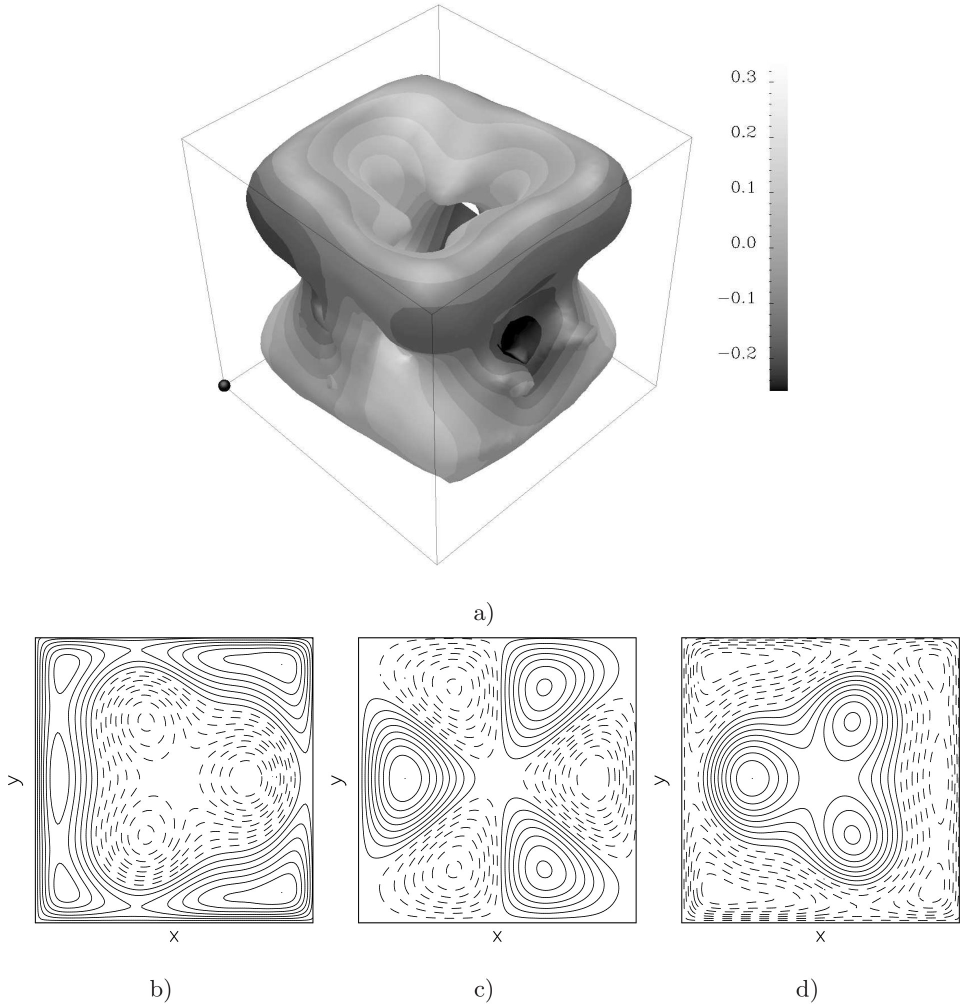

FIGURE 19. Stable B_{251} flow pattern at $Ra = 1.5 \times 10^5$ and Pr=130. (a) Surface of $\lambda_2 = 0$. The grey levels are scaled with the value of the vertical velocity component. Vertical velocity contours at the horizontal planes (b) $z = -0.25$, (c) $z = 0$ and (d) $z = 0.25$. Positive and negative values of the velocity are plotted with solid and dashed lines, respectively.

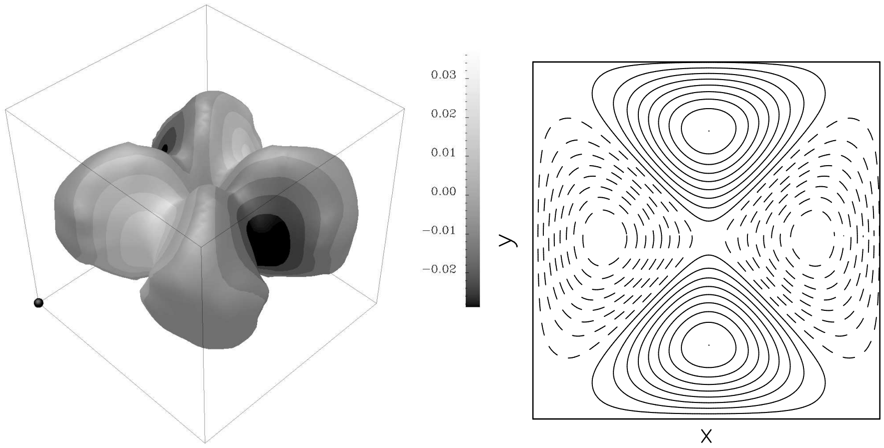

a) b)

FIGURE 20. Unstable B_5 flow pattern at $Ra = 1.5 \times 10^4$ and Pr=130. (a) Surface of $\lambda_2 = 0$. The grey levels are scaled with the value of the vertical velocity component. (b) Vertical velocity contours at the horizontal midplane $z = 0$. Positive and negative values of the velocity are plotted with solid and dashed lines, respectively.

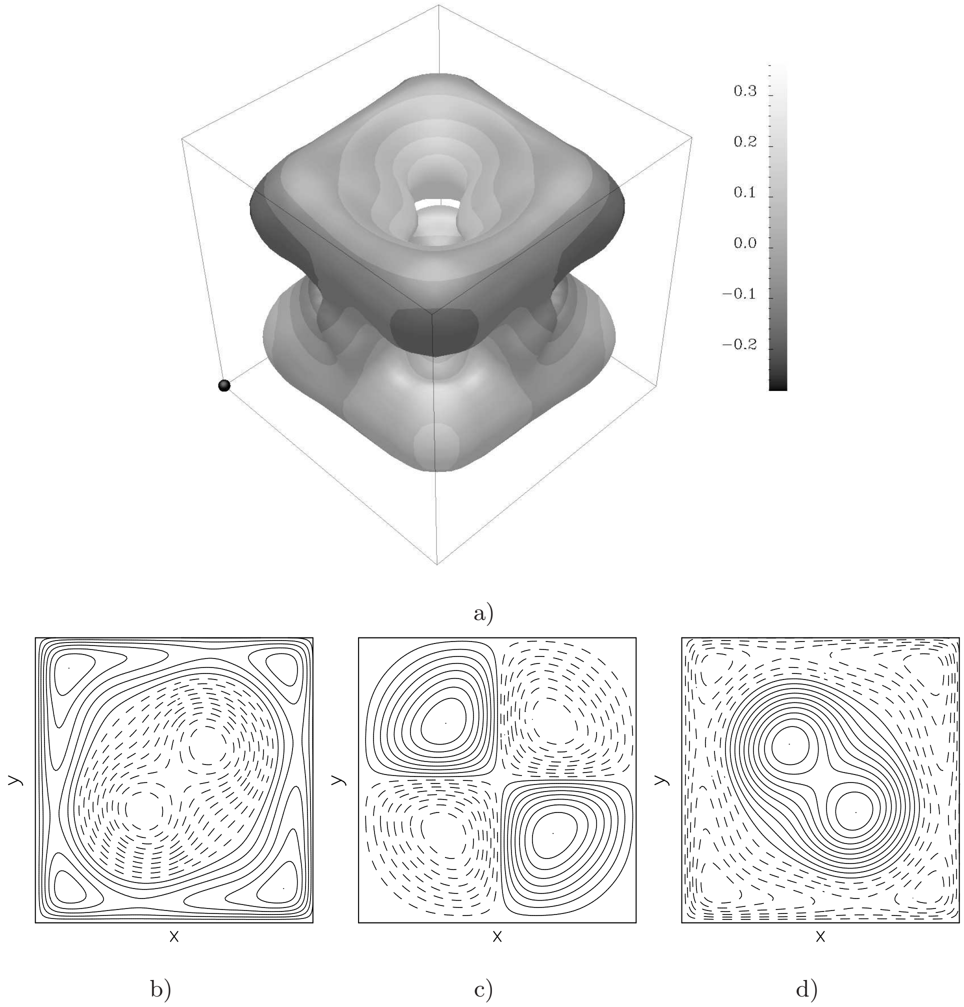

FIGURE 21. Unstable B_3 flow pattern at $Ra = 1.5 \times 10^5$ and Pr=130. (a) Surface of $\lambda_2 = 0$. The grey levels are scaled with the value of the vertical velocity component. Vertical velocity contours at the horizontal planes (b) $z = -0.25$, (c) $z = 0$ and (d) $z = 0.25$. Positive and negative values of the velocity are plotted with solid and dashed lines, respectively.

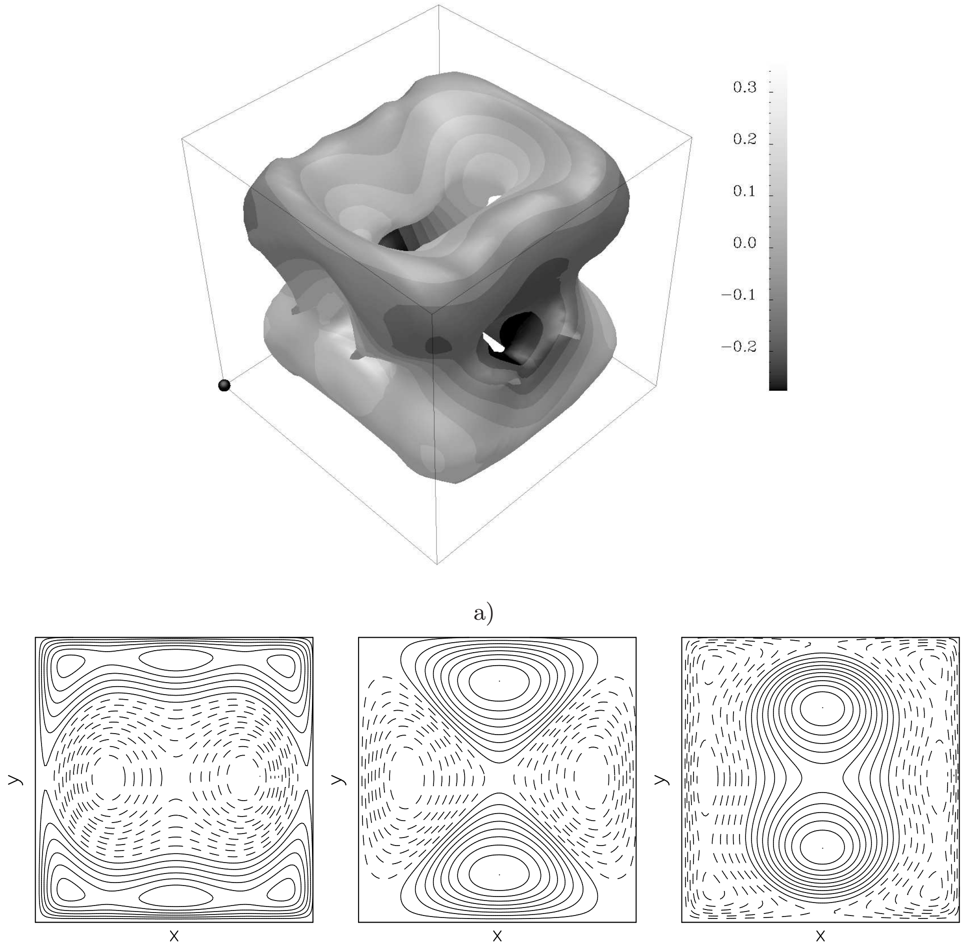

a)

b) c) d)

FIGURE 22. Stable B_5 flow pattern at $Ra = 1.5 \times 10^5$ and Pr=130. (a) Surface of $\lambda_2 = 0$. The grey levels are scaled with the value of the vertical velocity component. Vertical velocity contours at the horizontal planes (b) $z = -0.25$, (c) $z = 0$ and (d) $z = 0.25$. Positive and negative values of the velocity are plotted with solid and dashed lines, respectively.

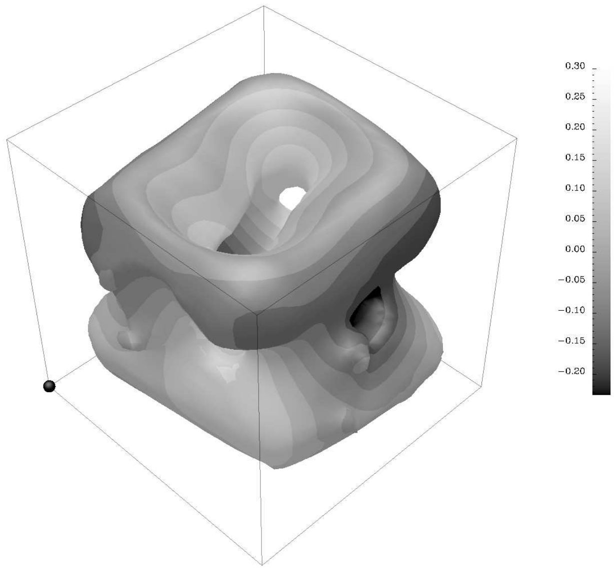

a)

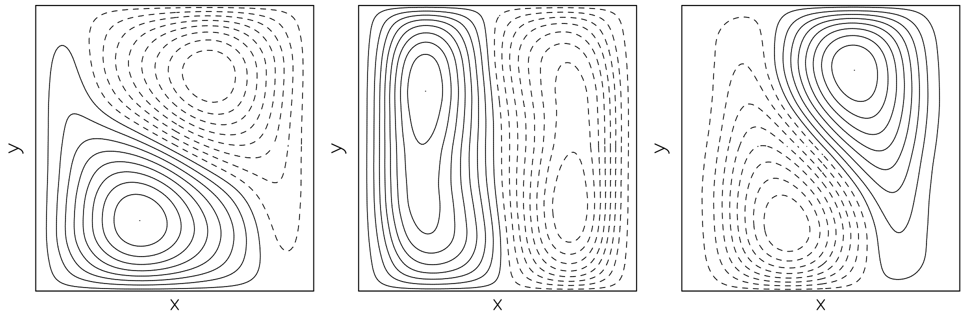

b) c) d)

FIGURE 23. Stable B_{34} flow pattern at $Ra = 8.7 \times 10^4$ and Pr=130. (a) Surface of $\lambda_2 = 0$. The grey levels are scaled with the value of the vertical velocity component. Vertical velocity contours at the horizontal planes (b) $z = -0.25$, (c) $z = 0$ and (d) $z = 0.25$. Positive and negative values of the velocity are plotted with solid and dashed lines, respectively.

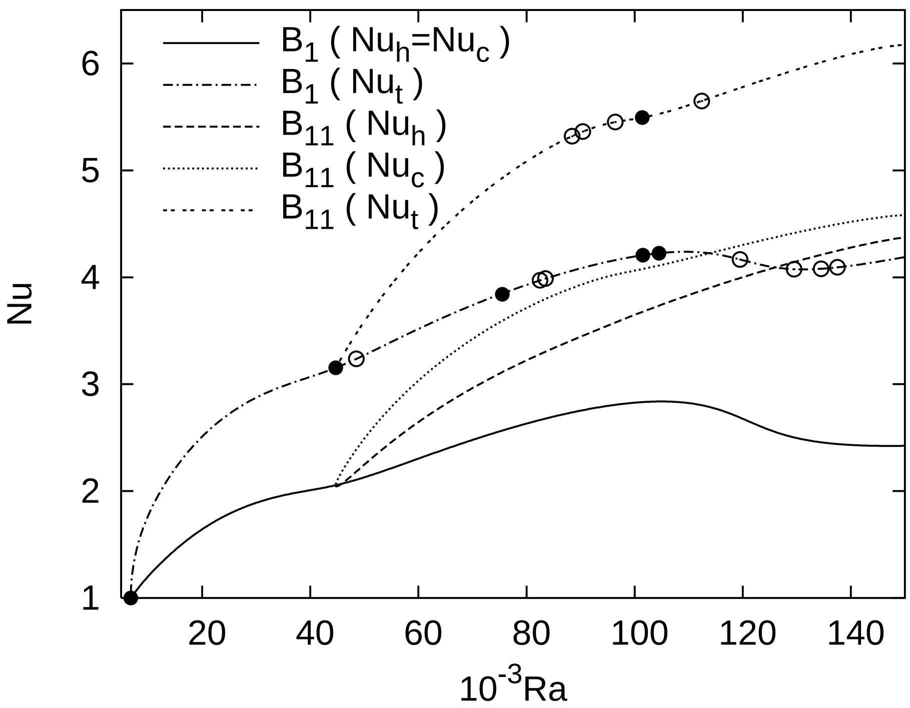

FIGURE 24. Variation of the Nusselt numbers Nu_h, Nu_c and Nu_t with respect to the Rayleigh number for the B_1 and B_{11} flow patterns at Pr=0.71). Steady and Hopf bifurcations are represented with filled and hollow circles, respectively.

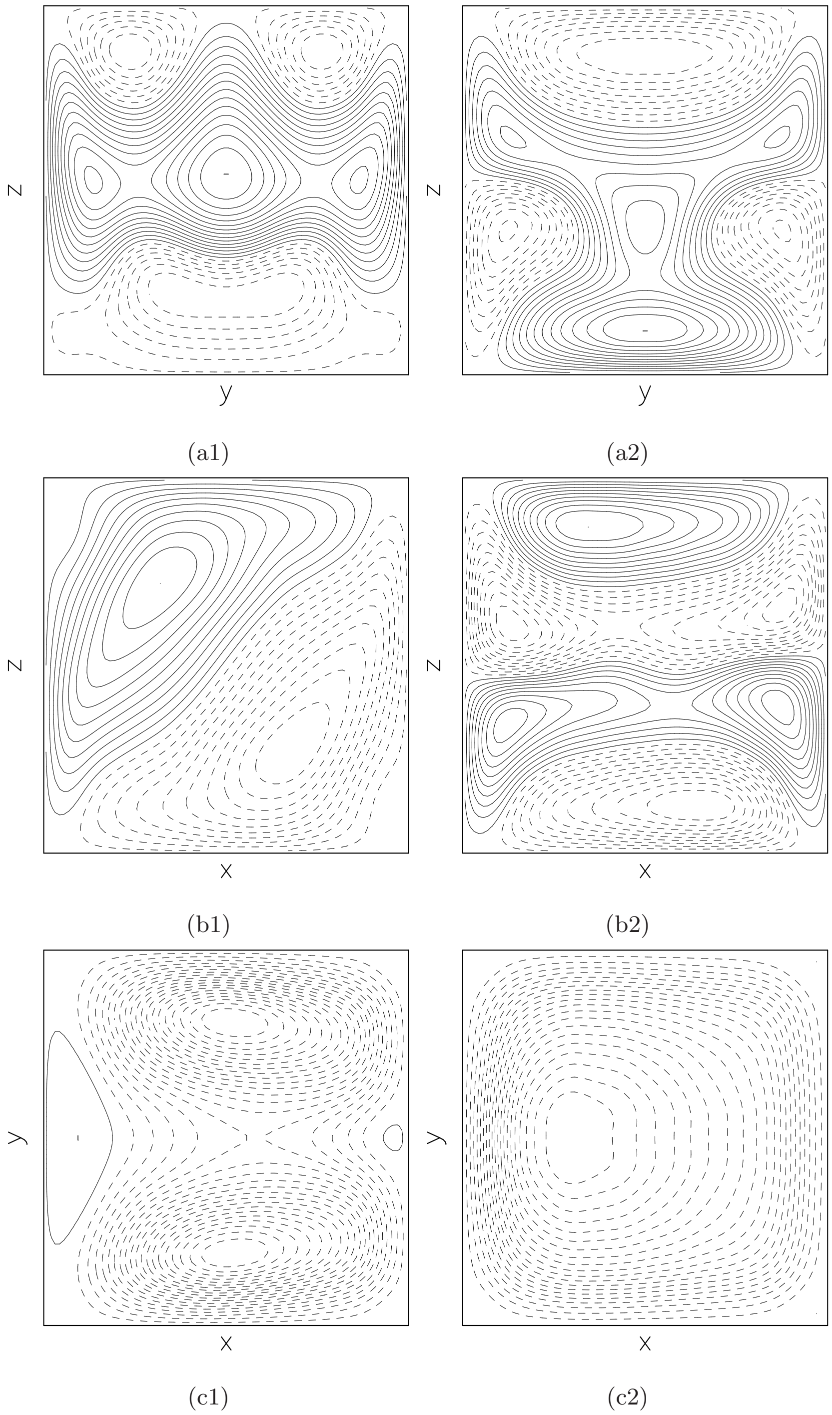

FIGURE 25. Local Nusselt, Nu_l, contours at lateral walls (a1-a2) $x = 1/2$, (b1-b2) $y = -1/2$ and (c1-c2) $z = 1/2$ for the B_1 flow pattern at $Ra = 1.5 \times 10^5$ at both Pr=0.71 (a1-c1) and Pr=130 (a2-c2). Positive and negative values of Nu_l are plotted with solid and dashed lines, respectively. Twenty–two equidistant contour lines are plotted in each figure. The maximum and minimum values in each figure are respectively -0.95, 2.26 (a1),-1.67, 2.63 (a2); -2.65, 2.65 (b1);-1.62, 1.62 (b2) and -4.46, 0.26 (c1); -8.06, 0.018(c2).

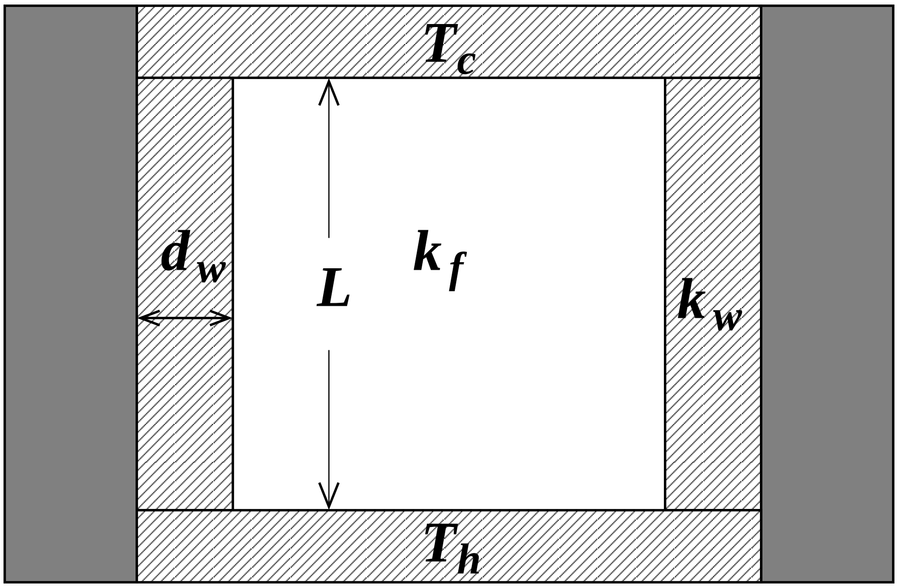

FIGURE 26. Sketch of a section of the physical device at $x = 0$. The dashed domains correspond to highly conducting walls. The bottom and top plates are kept to constant hot and cold temperatures T_h and T_c, respectively. The grey strips indicate that the lateral walls are insulated to prevent the lateral loss of heat from the device. The thermal conductivities of the fluid and the walls are k_f and k_w, respectively.

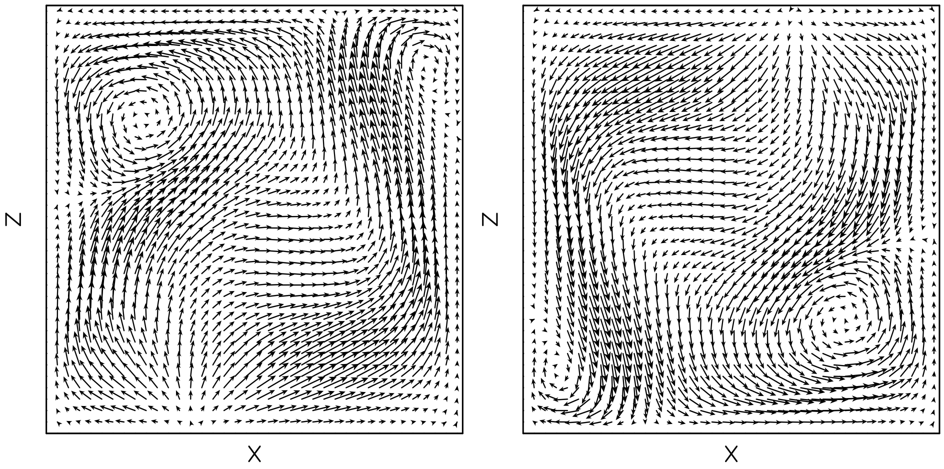

(a) (b)

FIGURE 27. (a, b) Projected velocity vectors at plane $y = 0$ for two realisations of B_{11} flow pattern at $Ra = 10^5$ and Pr=0.71.

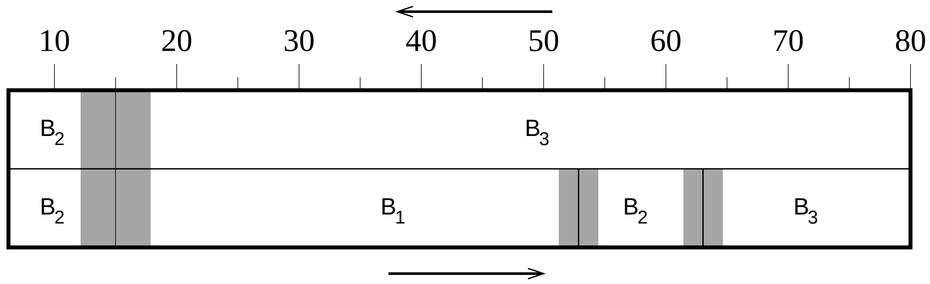

a)

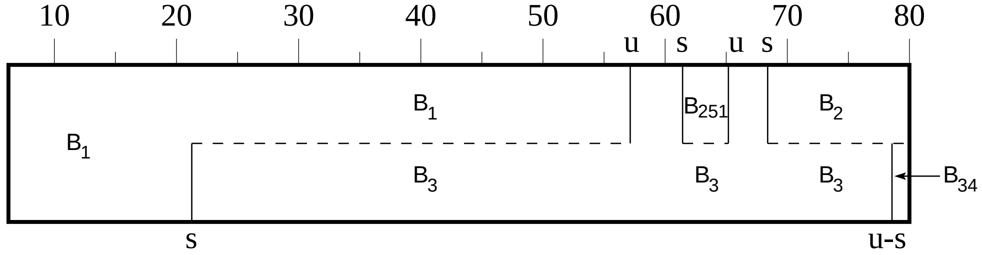

b)

FIGURE 28. (a) Sequence of flow transitions from the conductive state observed experimentally by Pallarès *et al.* (2001) when the Ra was increased and decreased stepwise (the experimental range of Ra where each transition occurred is indicated by grey strips). (b) Stable flow patterns identified by the current continuation method. Horizontal dashed lines indicate that both flow patterns printed above and below them are stable. Bifurcations are marked with vertical solid lines. Those bifurcation points where a flow pattern becomes stable or unstable are respectively labelled with s or u. The label u-s indicates that the initially stable flow pattern B_{34} sets in at the bifurcation point where the B_3 solution becomes unstable.

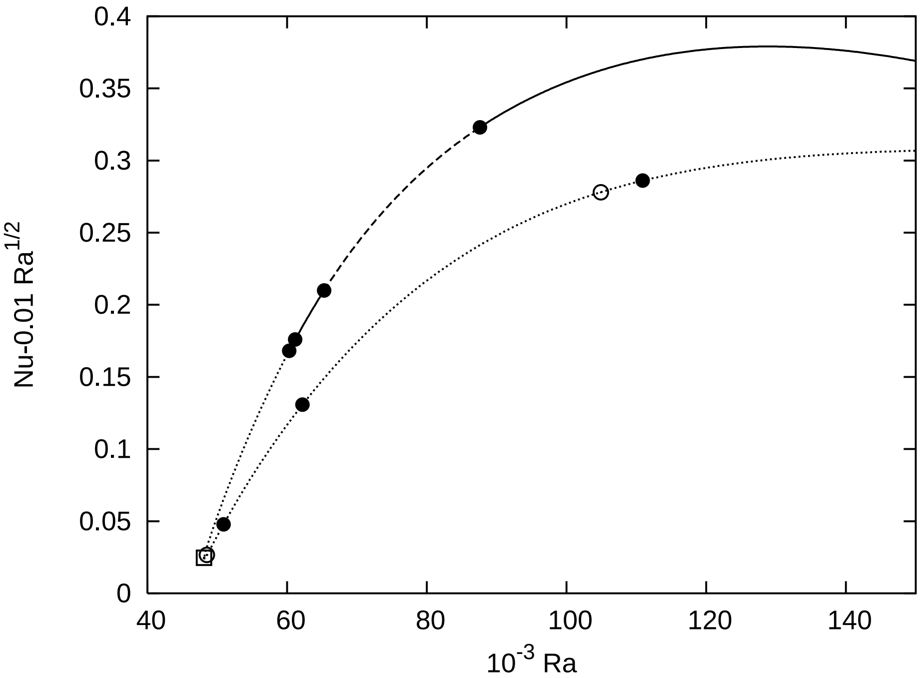

FIGURE 29. Variation of the Nusselt number with respect to the Rayleigh number for the B_{251} solution when the cavity is filled with silicone oil (Pr=130). The flow pattern is plotted with solid lines when it is stable. When the flow pattern is unstable it is plotted with dashed lines if it has exactly one unstable eigenmode and by dotted lines when it has two or more unstable eigenmodes. Steady bifurcations, Hopf bifurcations and turning points are represented by filled circles, hollow circles and hollow squares, respectively.

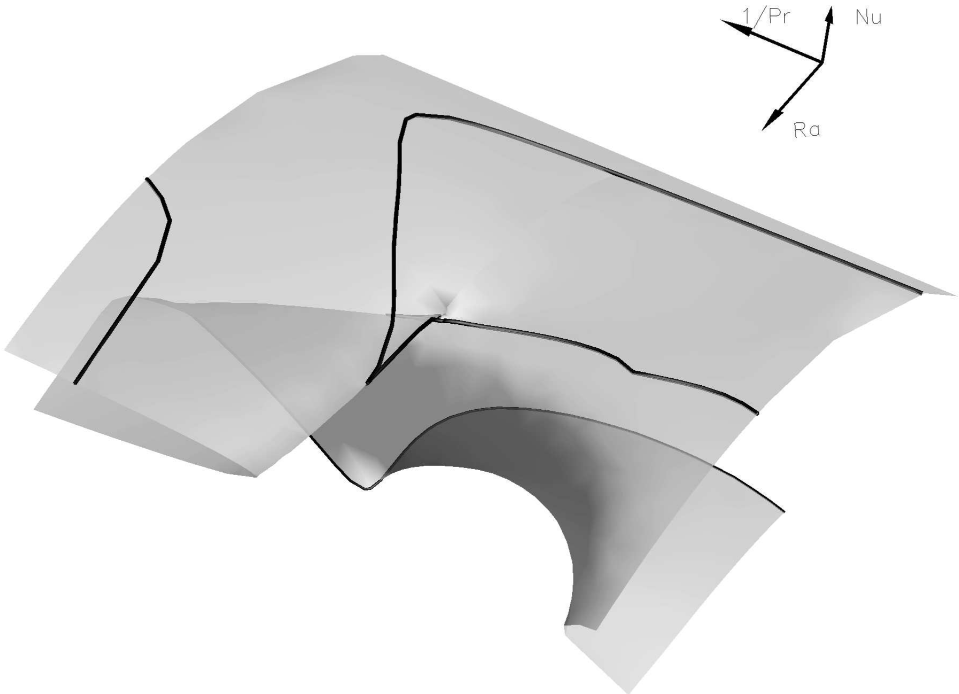

FIGURE 30. Variation of the Nusselt number with respect to the Rayleigh number and the inverse of the Prandtl number for the B_3 solution within the ranges $1.2 \times 10^4 \leqslant Ra \leqslant 1.2 \times 10^5$, $0.71 \leqslant Pr \leqslant 130$. The bifurcation curves where the stability character of the B_3 solution changes are depicted in black solid lines over the solution surface.

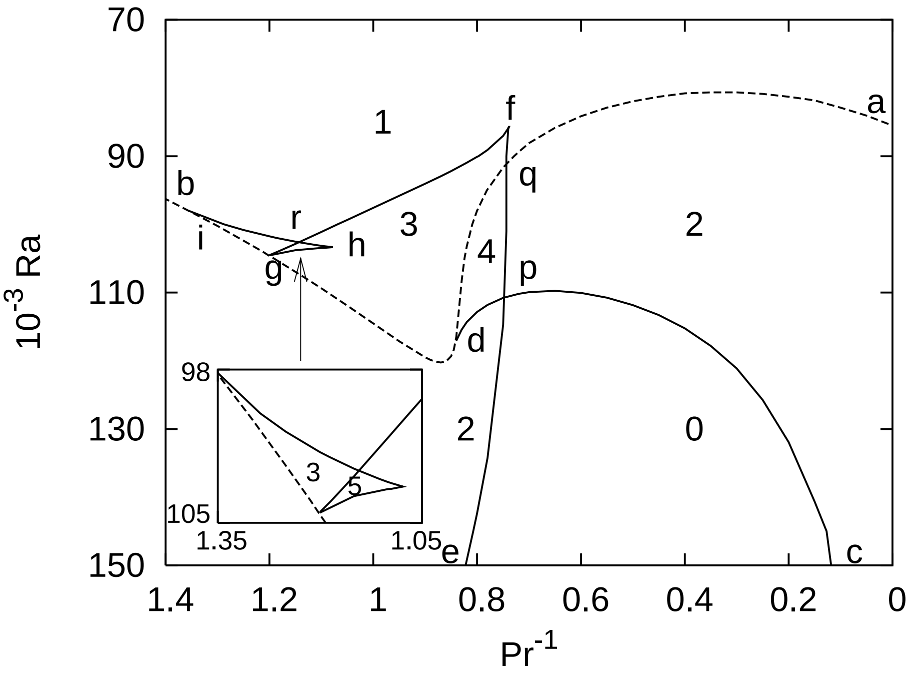

FIGURE 31. Parameter chart in the two dimensional (Ra,Pr^{-1}) plane for the B_3 solution. The curves plotted in this figure are bifurcation curves that separate regions in the plane where different number of realisations of the B_3 flow pattern are possible. The printed numbers indicate the number of possible realisations of the B_3 flow pattern within each region. Fold curves and symmetry-breaking bifurcation curves are plotted with solid and dashed lines, respectively. The directions of the axis in this figure are reversed to be consistent with axis in figure 30.

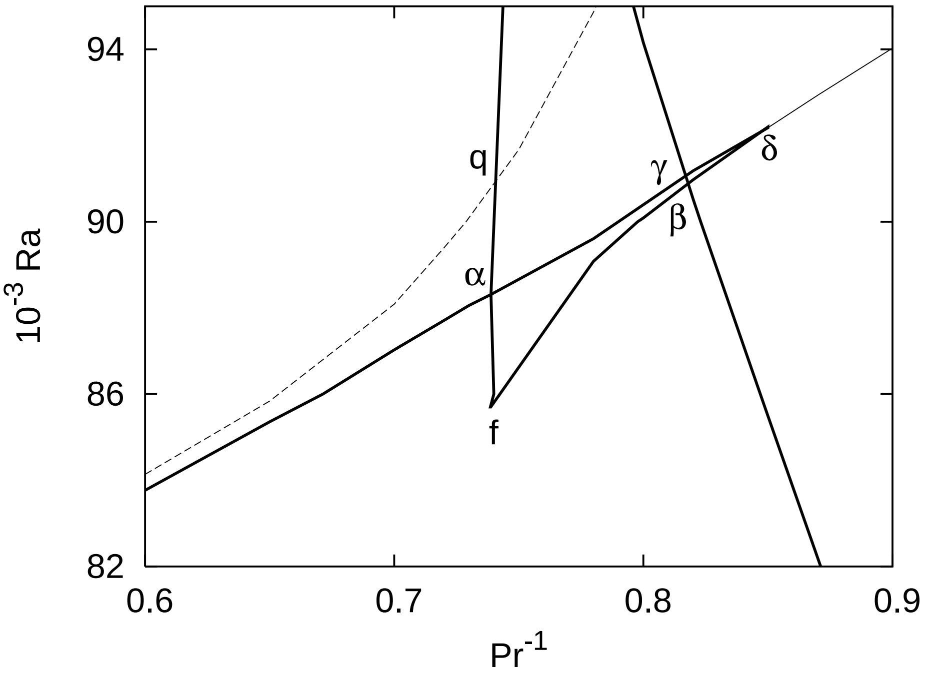

a)

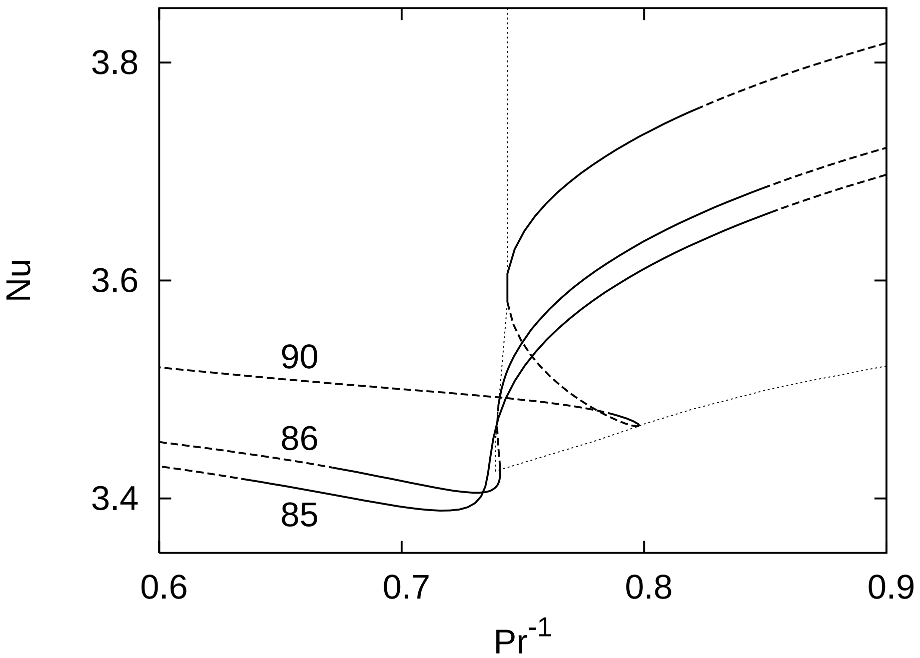

b)

FIGURE 32. a)The region α–δ–f is a region of stability for the B_3 flow pattern which is not properly seen in figure 30. The dashed line and the points labelled f and q correspond to the same line and points in the parameter chart plotted in figure 31. Two stable realisations of the B_3 flow pattern are stable within the region α–γ–β–f. b) Continuation curves over the B_3 solution surface at $Ra = 8.5 \times 10^4$, $Ra = 8.6 \times 10^4$ and $Ra = 9 \times 10^4$. The dotted curves correspond to the fold curves f–e and f–g in the parameter chart plotted in figure 31.

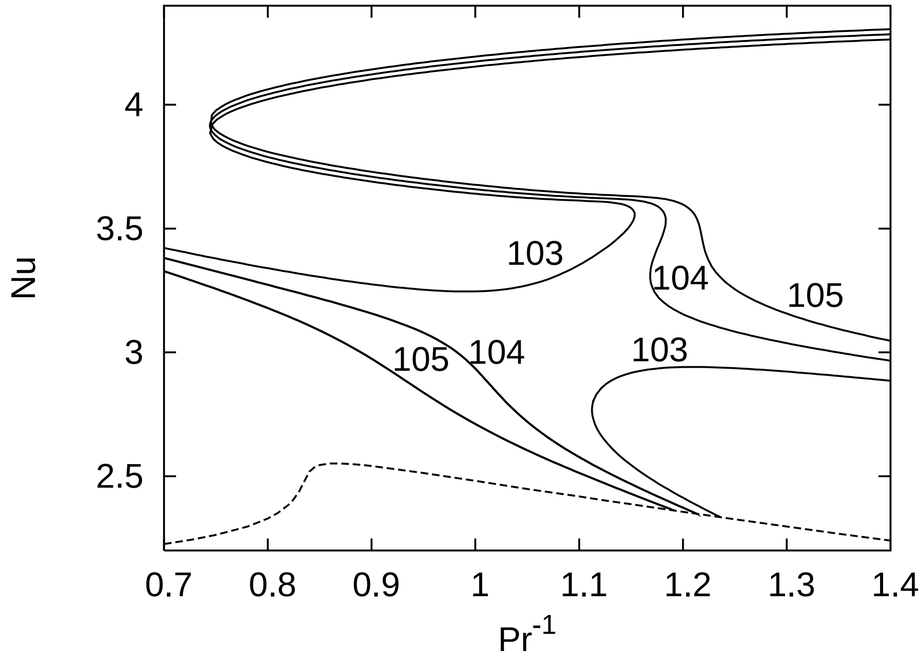

FIGURE 33. Development of the folds in the solution manifold near the cusp points g and h in figure 31. The curves plotted in this figure were obtained by a sequence of continuation runs using $1/Pr$ as a continuation parameter at three values of $10^{-3}Ra$, namely 103, 104 and 105. The dashed curve corresponds to the symmetry–breaking bifurcation curve in the parameter chart plotted in figure 31.